Title

Electrophysiological Mechanisms and Validation of Ferritin-Based Magnetogenetics for Remote Control of Neurons.

Journal

The Journal of Neuroscience, 44(30)

Authors

Hernández-Morales, Miriam

Morales-Weil, Koyam

Han, Sang Min

et al.

Publication Date

2024-07-24

DOI

10.1523/JNEUROSCI.1717-23.2024

Peer reviewed

Cellular/Molecular

Electrophysiological Mechanisms and Validation of Ferritin-Based Magnetogenetics for Remote Control of Neurons

Miriam Hernández-Morales,[1,2*] Koyam Morales-Weil,[1,2*] Sang Min Han,[1,2] Victor Han,[1,2] Tiffany Tran,[2] Eric J. Benner,[3] Kelly Pegram,[3] Jenna Meanor,[3] Evan W. Miller,[2,4,5] Richard H. Kramer,[5] and Chunlei Liu[1,2]

[1]Department of Electrical Engineering and Computer Sciences, University of California, Berkeley, California 94720, [2]Helen Wills Neuroscience Institute, University of California, Berkeley, California 94720, [3]Division of Neonatology, Department of Pediatrics, Duke University Medical Center, Jean and George Brumley, Jr. Neonatal-Perinatal Institute, Durham, North Carolina 27710, [4]Department of Chemistry, University of California, Berkeley, California 94720, and [5]Department of Molecular and Cell Biology, University of California, Berkeley, California 94720

Magnetogenetics was developed to remotely control genetically targeted neurons. A variant of magnetogenetics uses magnetic fields to activate transient receptor potential vanilloid (TRPV) channels when coupled with ferritin. Stimulation with static or RF magnetic fields of neurons expressing these channels induces Ca^{2+} transients and modulates behavior. However, the validity of ferritin-based magnetogenetics has been questioned due to controversies surrounding the underlying mechanisms and deficits in reproducibility. Here, we validated the magnetogenetic approach Ferritin-iron Redistribution to Ion Channels (FeRIC) using electrophysiological (Ephys) and imaging techniques. Previously, interference from RF stimulation rendered patch-clamp recordings inaccessible for magnetogenetics. We solved this limitation for FeRIC, and we studied the bioelectrical properties of neurons expressing TRPV4 (nonselective cation channel) and transmembrane member 16A (TMEM16A; chloride-permeable channel) coupled to ferritin (FeRIC channels) under RF stimulation. We used cultured neurons obtained from the rat hippocampus of either sex. We show that RF decreases the membrane resistance (Rm) and depolarizes the membrane potential in neurons expressing $TRPV4^{FeRIC}$. RF does not directly trigger action potential firing but increases the neuronal basal spiking frequency. In neurons expressing $TMEM16A^{FeRIC}$, RF decreases the Rm, hyperpolarizes the membrane potential, and decreases the spiking frequency. Additionally, we corroborated the previously described biochemical mechanism responsible for RF-induced activation of ferritin-coupled ion channels. We solved an enduring problem for ferritin-based magnetogenetics, obtaining direct Ephys evidence of RF-induced activation of ferritin-coupled ion channels. We found that RF does not yield instantaneous changes in neuronal membrane potentials. Instead, RF produces responses that are long-lasting and moderate, but effective in controlling the bioelectrical properties of neurons.

Key words: **ferritin; magnetogenetics; membrane potential; neuromodulation; TMEM16A; TRPV4**

Significance Statement

Cell-specific and noninvasive stimulation can be a powerful tool for modulating neuronal circuits and functions. Magnetogenetic techniques that are fully genetically encoded provide such tools. However, there have been significant controversies surrounding the efficacy and underlying mechanisms of magnetogenetics. Here, we demonstrate that by employing a fully genetically encoded magnetogenetic approach called FeRIC, we can modulate neuronal voltage, inducing either depolarization or hyperpolarization through the activation of ion channels with magnetic fields; we validate this modulation mechanism with the gold-standard patch-clamp technique. We further discover that this neuronal modulation is not achieved by instantaneously triggering action potentials as previously assumed, but by modulating neuronal excitability.

Received Sept. 7, 2023; revised May 7, 2024; accepted May 10, 2024.

Author contributions: M.H-M., K.M-W., V.H., E.J.B., and C.L. designed research; M.H-M., K.M-W., V.H., T.T., E.J.B., K.P., J.M., and C.L. performed research; E.J.B., K.P., E.W.M., and R.H.K. contributed unpublished reagents/analytic tools; M.H-M., K.M-W., S.M.H., V.H., T.T., and C.L. analyzed data; M.H-M. wrote the paper.

Research reported in this publication was, in part, supported by the National Institute of Neurological Disorders and Stroke of the National Institutes of Health under Award Number R01NS110554.

*M.H-M. and K.M-W. contributed equally to this work.

E.J.B and C.L. share ownership of a patent application (WO2016004281 A1 PCT/US2015/038948) relating to the use of Ferritin-iron Redistribution to Ion Channels for cell modulation and treatments. All other authors declare no competing financial interests.

Correspondence should be addressed to Chunlei Liu at chunlei.liu@berkeley.edu.

https://doi.org/10.1523/JNEUROSCI.1717-23.2024

Introduction

Magnetogenetics aims to manipulate the activity of genetically targeted cells with magnetic fields. Low to midfrequency (kHz and MHz) magnetic fields are safe and penetrate through tissues (Young et al., 1980; Schenck, 2000), allowing noninvasive and on-demand control of cell activity. Some magnetogenetic approaches use the transient receptor potential vanilloid (TRPV) 1 and 4 channels coupled with ferritin as magnetic actuators (Stanley et al., 2016; Wheeler et al., 2016; Hutson et al., 2017; Duret et al., 2019; Brier et al., 2020; Hernández-Morales et al., 2020, 2021). TRPV1 and TRPV4 are nonselective cation channels activated by heat, pH changes, mechanical stimuli, and endogenous lipids (Caterina et al., 1999; Voets et al., 2002; Watanabe et al., 2003; Darby et al., 2016; Benítez-Angeles et al., 2020). Ferritin, an iron storage protein, transduces magnetic fields into stimuli that activate the coupled TRPV channels. While initial studies proposed that ferritin transduces static and radiofrequency (RF) magnetic fields into a thermal stimulus (Wheeler et al., 2016; Duret et al., 2019), other studies suggested that this effect is insufficient to activate the temperature-sensitive ion channels (Meister, 2016; Davis et al., 2020). We and others found that ferritin transduces RF magnetic fields into biochemical stimuli (Brier et al., 2020; Hernández-Morales et al., 2020). RF produces a ferritin-dependent increase in free cytosolic iron levels with a subsequent production of reactive oxygen species (ROS) and oxidizes lipids that activate the ferritin-coupled TRPV channels (Brier et al., 2020; Hernández-Morales et al., 2020). Several studies reported the magnetic activation of ferritin-coupled TRPV1 and TRPV4 in vitro and in vivo (Stanley et al., 2016; Wheeler et al., 2016; Hutson et al., 2017; Duret et al., 2019; Hernández-Morales et al., 2020, 2021). Because these channels are permeable to Ca^{2+}, the magnetic field-induced activation has been examined by monitoring the cytosolic Ca^{2+} levels (Stanley et al., 2015, 2016; Wheeler et al., 2016; Hutson et al., 2017; Duret et al., 2019; Brier et al., 2020; Hernández-Morales et al., 2020, 2021) or by detecting the expression of Ca^{2+}-responsive genes (Stanley et al., 2015, 2016). The magnetic control of neurons has also been examined by monitoring the behavioral output of animals such as the escape response and coiling behavior in zebrafish (Wheeler et al., 2016) and feeding behavior in mice (Stanley et al., 2016; Wheeler et al., 2016). Although these studies indirectly indicate that magnetic fields activate ferritin-coupled ion channels, the field of magnetogenetics has been under controversy due to the lack of direct, definitive evidence showing the activation of these channels.

For example, one study reported that stimulating neurons expressing Magneto2.0, a ferritin-fused TRPV4, with static magnetic fields triggers action potential (AP) firing (Wheeler et al., 2016). However, a series of independent studies using electrophysiological (Ephys) recordings reported that magnetic stimulation failed to trigger AP firing and did not change the electrical properties of multiple types of neurons expressing Magneto2.0 (Kole et al., 2019; Wang et al., 2019; Xu et al., 2019). These contradictory results added uncertainty to the field of magnetogenetics. In addition to these refutations, there has been no direct Ephys evidence for the activation of the TRPV channels under RF stimulation. This lack of evidence has been in part due to the technical challenge posed by electromagnetic interference between the RF and the Ephys setups. Here, we solved this problem and obtained direct Ephys evidence of the RF-induced activation of ion channels coupled with ferritin. Specifically, we employed the technique called Ferritin-iron Redistribution to Ion Channels (FeRIC) that uses TRPV4 and transmembrane member 16A (TMEM16A) fused with the ferritin-binding domain 5 (D5) of kininogen to be coupled with endogenous ferritin, called FeRIC channels. We show that RF activates the nonselective cation channel $TRPV4^{FeRIC}$ and the chloride-permeable channel $TMEM16A^{FeRIC}$, producing opposite effects on the membrane potential, excitability, and neuronal spiking frequency. Our results provide direct Ephys evidence that resolves the controversy and supports magnetogenetics as a valid and viable technique for modulating neuronal bioelectrical properties.

Materials and Methods

Experimental design

All animal experiments were approved by the Duke University Animal Care and Use Committee and the University of California (UC) Berkeley Animal Care and Use Committees and in accordance with the National Institutes of Health (NIH) Guide for the Care and Use of Laboratory Animals and the Public Health Policy.

Cell lines

Neuro2a cell line (N2a, ATC, CCL-13) was used. N2a cells were obtained from the UCB Cell Culture Facility. Cell identity and negative *Mycoplasma* contamination were verified by the UCB Cell Culture Facility. Cells were maintained in Dulbecco's modified Eagle's medium (DMEM; Invitrogen) supplemented with 10% fetal bovine serum (FBS; Hyclone) and 100 units/ml penicillin and 100 mg/ml streptomycin at 37°C and 5% CO_2.

Primary neuron cultures

Rat hippocampal neurons were obtained as previously described (Huang et al., 2015; Walker et al., 2021). Hippocampi were dissected from embryonic Day 18 Sprague–Dawley rats of either sex (Charles River Laboratories) and maintained in Hanks balanced salt solution (HBSS; Invitrogen #14170112). The hippocampal tissue was enzymatically treated with 2.5% trypsin (15 min at 37°C). Next, the tissue was mechanically dissociated using a fire-polished Pasteur pipette in minimum essential medium (MEM; Invitrogen #11090-081) supplemented with 5% FBS, 2% B-27 (Invitrogen #17504044), 2% D-glucose, and 1% GlutaMAX (Invitrogen # 35050061). Cells were plated onto poly-D-lysine (1 mg/ml, Sigma #P0899)-coated coverslips (12 mm) at 6×10^4 cells/cm^2 in a MEM-supplemented medium. After 24 h, 50% of the MEM-supplemented medium was replaced with a Neurobasal medium (Invitrogen #21103-049) supplemented with 2% B-27 and 1% GlutaMAX. Cells were maintained at 37°C and 5% CO_2. Experiments using cultured hippocampal neurons were conducted between 12 and 14 d after seeding because at this time, cultured neurons have established circuits (Sun et al., 2018).

Plasmids

The constructs $TRPV4^{FeRIC}$ and $TRPV4^{WT}$ were obtained as described previously (Hutson et al., 2017). To generate the $TRPV4^{WT}$ construct, we used full-length rat TRPV4 cDNA, which was a gift from R. Lefkowitz (Duke University). Spe I and Not I restriction sites were introduced using PCR. The full-length wild-type (WT) TRPV4 was subcloned into the PLVX-IRES-mCherry vector to generate $TRPV4^{WT}$ (Clontech, Catalog No. 631237). To generate the $TRPV4^{FeRIC}$ construct, PCR primers were designed to eliminate the 3′ stop site in WT TRPV4 and introduce a 3′ Not I site. PCR primers introducing a 5′ Not I site and a 3′ BamH I site and a stop codon were used to amplify human Kininogen1 D5 (FeRIC). This FeRIC fragment was subcloned into the Xba I and BamH 1 sites within the PLVX-IRES-mCherry vector containing TRPV4. To generate the $TMEM16A^{WT}$ construct, we used full-length TMEM16A cDNA, which was obtained from OriGene (mouse-untagged clone, PCMV6-Kan/Neo, #MC205263). TMEM16A cDNA was subcloned into the PLVX-IRES-mCherry vector between the 5′ Not I and 3′ BamH I sites. To generate $TMEM16A^{FeRIC}$, PCR primers were designed to introduce the 5′ EcoR I and the 3′ Not I and to eliminate the stop codon in the FeRIC (human Kininogen1 D5) fragment. This FeRIC fragment was

subcloned into the EcoR I and Not I sites within the PLVX-IRES-mCherry vector containing TMEM16A. All completed constructs were sequence-verified by the Molecular Cell Biology Sequencing Facility (UC Berkeley) and analyzed using Serial Cloner 2.6 and Benchling.

Chemical transfection of N2a cells

N2a cells were plated on noncoated 12 mm coverslips placed into four-well plates. Cells were seeded at a density of $2.5–5 \times 10^3$ cells/coverslip and cultured in a DMEM-supplemented medium. After 18–24 h, cells were transfected using the Lipofectamine LTX PLUS reagent (Thermo Fisher Scientific #15338030) with WT or FeRIC channels. For imaging experiments, N2a cells were cotransfected with the WT or FeRIC channels and GCaMP6 (GCaMP6 medium, Addgene, Catalog No. 40754) or YFP-H148Q. For transfection, OptiMEM-free serum medium (Thermo Fisher Scientific #31985088) was used to prepare the DNA/Lipofectamine LTX mix. The transfection mix had the following composition per 35 mm dish: 300 µl OptiMEM, 4 µl Lipofectamine LTX, 3 µl PLUS reagent, 0.7 µg ion channel DNA, and 0.7 µg of GCaMP6 DNA. The transfection mix had the following composition per 12 mm coverslip into 24-well plates: 100 µl OptiMEM, 1 µl Lipofectamine LTX, 1 µl PLUS reagent, 0.2 µg ion channel DNA, and 0.2 µg of indicator DNA.

Chemical transfection of cultured neurons

Neurons plated on 12 mm coverslips were seeded at 7×10^4 cells/cm^2 and cultured in a Neurobasal-supplemented medium. After 8–14 d, cells were transfected using the Lipofectamine 2000 (Thermo Fisher Scientific #11668019) with GCaMP6 (GCaMP6 medium, Addgene, Catalog No. 40754) and the FeRIC channels. For transfection, OptiMEM-free serum medium (Thermo Fisher Scientific #31985088) was used to prepare the DNA/Lipofectamine 2000 mix. The transfection mix had the following composition per coverslip/well: 100 µl OptiMEM, 2 µl Lipofectamine 2000, 0.5–0.7 µg FeRIC channel DNA, and 0.5 µg of GCaMP6 DNA. Neurons were incubated with the transfection mix at 37°C for 3 h. Next, the culture medium containing the transfection mix was replaced with a fresh Neurobasal-supplemented medium. Experiments were conducted 3–4 d after transfection.

RF coil

The RF-emitting coil consisted of a single loop of wire with a loop diameter of ∼2.8 or 5 cm. The coil was connected in parallel with tuning capacitors, forming an LC circuit resonant near 180 MHz. The circuit was matched to ∼50 Ω near 180 MHz using a series capacitor. The coil was checked to still be matched near 180 MHz when parasitic capacitance due to the nearby metal (e.g., from a microscope) was present. The RF signal was generated by a broadband (35 MHz to 4.4 GHz) signal generator (RF Pro Touch, Red Oak Canyon) and amplified using a 5 W amplifier (Amplifier Research, model 5U100, 500 kHz to 1,000 MHz). The magnetic field produced by the coils was measured using EMC near-field probes (Beehive Electronics model 100B) connected to a spectrum analyzer (RSA3015E-TG, RIGOL Technologies). The Beehive 100B probe was provided with magnetic field calibration data from the manufacturer, and proper scaling factors for 180 MHz measurements were interpolated based on this data. The RIGOL spectrum analyzer was manufacturer calibrated with a system registered to ISO9001:2008. Using the Beehive probe and the RIGOL spectrum analyzer, the magnetic field strength was measured to be ∼1.6 µT for 180 MHz at a location ∼3 mm above the recording chamber. Unless stated otherwise, these are the values used throughout the manuscript. The measurements were made slightly above the cell culture dish location because the probes could not be lowered into the coils without changing the angle of the probes with respect to the magnetic field.

To ensure that the coaxial cables connected to the RF coil did not act as antennas producing unwanted RF interference, two ferrite beads designed to block frequencies near 180 MHz (Laird-Signal Integrity Products manufacturer part number 28A0592-0A2) were placed on the cables. This was especially important because without the ferrite beads, when the RF stimulus was turned on, the shift in basal current levels on the Ephys recordings increased by several orders of magnitude, and large RF signals could be picked up in the air by a spectrum analyzer and a loop probe far away from the RF coil.

Measurements of the voltage or current basal shift produced by an RF source

RF voltages induced on the headstage are transmitted into the Ephys recordings in the form of a baseline shift. The baseline shift was measured as a function of the RF magnetic field produced by a 2.8 cm diameter coil pipette under in-the-bath conditions or as a function of RF voltage produced by a Siglent SDG6022X arbitrary waveform generator directly connected (for the current-clamp configuration) or capacitively coupled (for the voltage-clamp configuration) to the headstage. In the case of directly/capacitively coupled connections, a voltage source and a series 50 Ω resistance, corresponding to the waveform generator and its output impedance, respectively, were connected directly to the headstage. A 50 Ω characteristic impedance cable of ∼2 ft was situated between the waveform generator and the headstage. Given the 50 Ω output impedance, the power and thus the voltage delivered to the headstage are not dependent on the length of the cable, except for minor losses negligible for short cable lengths. For voltage-clamp measurements, in order to present a large low-frequency impedance to the headstage and prevent the headstage from attempting to provide large currents, a 10 pF capacitor (Johanson Technology 102S42E100JU3S) was placed in series between the headstage and the cable immediately next to the headstage. This capacitance passes the RF from the waveform generator to the headstage while blocking static currents between the waveform generator and the headstage.

Using a MultiClamp 700A amplifier (Axon Instruments), we measured the baseline shift in picoampere for the voltage-clamp configuration or the baseline shift in millivolt for the current-clamp configuration as a function of RF voltage on the voltage source from the waveform generator. The data were fit with one-term polynomials.

Ca^{2+} imaging

Epifluorescence imaging experiments were conducted as previously described (Hernández-Morales et al., 2020, 2021). Cytosolic levels of Ca^{2+} were monitored by fluorescence imaging of cells positive for GCaMP6. Cells expressing FeRIC channels were identified as those cells with mCherry-positive expression. Experiments were conducted using an upright Axio Examiner Z-1 (Zeiss) equipped with a camera (Axiocam 702 mono) controlled by Zen 2.6 software. Excitation light was delivered from a LED unit (33 W/cm^2; Colibri 7, Type RGB-UV, Zeiss). mCherry was excited at 590/27 nm and emission was collected at 620/60 nm. GCaMP6 was excited at 469/38 nm and emission was collected at 525/50 nm. Illumination parameters were adjusted to prevent overexposure and minimize GCaMP6 photobleaching. All experiments corresponding to a series were done under the same illumination settings. Images were captured with a W "Plan-Apochromat" 20×/1.0 DIC $D = 0.17$ M27 75 mm lens at one frame/s. Experiments were carried out at room temperature (20–22°C) using HBSS (Invitrogen, 14025092). At the beginning of imaging experiments, cells were washed three times with 1 ml of the HBSS. Next, the dish was placed onto the microscope stage, and the cells were localized with transmitted illumination (bright-field). Next, with reflected illumination, the fluorescence signals from mCherry and GCaMP6 were corroborated, and the field of view of interest was selected. Preferred fields of view were those with isolated and healthy cells. A thermocouple coupled to a thermistor readout (TC-344C, Warner Instruments) was placed inside the plate in direct contact with the HBSS. The temperature of the HBSS was monitored during the experiment (initial temperature, 22.09°C; final temperature, 22.03°C; ΔT, −0.6°C; $n = 305$). Cells were rested for ∼10 min before imaging. RF was delivered using a custom-built RF-emitting coil. Cells were stimulated with RF fields at 180 MHz (at 1.6–10 µT). For each experiment, cells were imaged for the first 60–120 s with no stimulus (basal) and followed by RF exposure.

Voltage imaging—BeRST 1

Neurons previously transfected with either FeRIC or WT channels were incubated with an imaging solution (Invitrogen) containing BeRST (500 nM) at 37°C for 20 min. Neurons expressing the FeRIC or WT channels were identified as those positive for mCherry. Fluorescence imaging of BeRST 1 was conducted on the Axio Examiner Z-1

microscope described above. Images were acquired with a W-Plan-Apo 20×/1.0 water objective (20×; Zeiss) at one frame/20 ms. mCherry images were acquired as described above. BeRST 1 was excited at 640/30 nm and emission was collected at 690/50 nm. Images were analyzed using ImageJ (NIH). Regions of interest were placed over the soma of neurons. Responses are presented as $\Delta F/F_0$, where F_0 is the resting fluorescence averaged over the first 100 frames at the start of acquisition. Customized code (MATLAB) was developed to analyze data and automatically compute the neuronal spiking frequency.

Ephys recordings

The electrical properties of cells were examined using the patch-clamp technique in the whole-cell configuration. Cells were transferred to a recording chamber filled with extracellular saline solution and placed on the microscope stage (Axio Examiner Z-1, Zeiss). N2a cells were recorded using HBSS (Thermo Fisher Scientific™ 14025-092), and cultured neurons were recorded using live cell imaging solution (Invitrogen™ A14291DJ) supplemented with 5 mM glucose. Whole-cell recordings were performed from the soma of N2a or hippocampal neurons with patch pipettes with a resistance between 4 and 8 MΩ. In voltage-clamp experiments, the holding voltage (V_h) was adjusted to −60 mV, and the capacitive currents were compensated up to 70%. For experiments with TRPV4 channels, the internal solution contained the following (in mM): 135 $KmeSO_4$, 10 KCl, 10 HEPES-K^+, 5 NaCl, 5 ATP-Mg^{2+}, and 0.4 GTP-Na^+, pH 7.2–7.3. The estimated equilibrium potentials were as follows (in mV): 82 Na^+, −84 K^+, 120 Ca^{2+}, and −57 Cl^-. Because TRPV4 is permeable to Na^+, K^+, and Ca^{2+}, its reversal potential is governed by these three conductances and has a value ranging from 0 to 10 mV. For experiments with TMEM16A channels, we set the chloride equilibrium potential at −98 mV by using a low chloride internal solution. This increases the chloride driving force, facilitating the observation of TMEM16A activation. The low chloride internal solution contained the following (in mM): 145 $KmeSO_4$, 10 HEPES-K^+, 3 NaCl, 5 ATP-Mg^{2+}, and 0.4 GTP-Na^+, pH 7.2–7.3. The voltage-clamp recordings were performed using a Patch-Clamp PC-501A (Warner Instruments) or a MultiClamp 700A amplifier (Axon Instruments). Experiments were accepted if the seal resistance was greater than 1 GΩ and the access resistance (Ra; ∼10–30 MΩ) did not change >20% during the span of the experiment. The Ra was monitored by applying a voltage step (−5 mV, 200 ms). This strategy offers the advantage of simultaneously monitoring the membrane resistance (Rm) and the Ra to rule out the possibility of observing changes in Rm due to changes in the patch-clamp seal quality. Experiments included in the analysis are those where Ra did not change >20% with respect to the baseline during the span of the experiment. Currents elicited by the −5 mV voltage pulse were measured to calculate the Rm. To obtain the voltage versus current (V–I) relation in N2a cells recorded in voltage-clamp mode, 12 voltage steps (1 s duration, −80 to −25 mV, $\Delta V = 10$ mV) were applied. For neurons recorded in current-clamp mode, the membrane potential was set by injecting current, and the Rm was monitored during the experiments with a current pulse (−5 pA, 500 ms). To obtain the current versus voltage (I–V) relation in neurons, 12 current pulses (1 s duration, −20 to 80 pA, $\Delta I = 10$ pA) were applied. To assess the effects of RF on neuronal Ephys properties, I–V relations were characterized in resting conditions and after 5 min of RF stimulation. Data were acquired with a low-pass filter with cutoff frequency set at 3.0 kHz and sampled at 10.0 kHz using an A/D converter Digidata 1320A (Axon Instruments) or Axon Digidata 1550B (Molecular Devices). Digidata 1320A with pClamp 10.7 software (Molecular Devices) and Axon Digidata 1550B with pClamp 11.2 software (Molecular Devices) were used to acquire data and generate the current pulses and voltage steps.

Cell viability and plasma membrane integrity assay

Cell viability was measured with the LDH-Glo™ Cytotoxicity Assay (Promega, #J2380). The assay measures the amount of lactate dehydrogenase (LDH) enzyme released from cells into the extracellular space (culture medium) when the plasma membrane loses its integrity. LDH participates in chemical reactions with the LDH-Glo™ Cytotoxicity Assay reagents producing a luminescent product.

N2a cells were plated on noncoated 12 mm coverslips placed into four-well plates. Cells were seeded at a density of 2.5×10^3 cells/coverslip and cultured in a DMEM-supplemented medium at 37°C and 5% CO_2. After 18–24 h, cells were transfected using the Lipofectamine LTX PLUS reagent (Thermo Fisher Scientific #15338030) with FeRIC channels. At 24 h post-transfection, the culture medium of seeded cells was sampled (5 µl) and the LDH levels were measured. Cells then underwent a 10 min RF stimulation (180 MHz and 10 µT). Control experiments involved placing cells in the same room concurrently with RF-stimulated cells, but in a location where RF stimulation was absent. Twenty-four hours after cells were stimulated with RF, the culture medium was sampled and the LDH levels were measured. To ensure LDH measurement reproducibility, control experiments were performed using the culture medium from unseeded wells under identical experimental conditions to those with seeded cells. The LDH measurement was conducted following the manufacturer's protocol. Reactions were set using dark optical polystyrene polymer bottom 96-well plates (Thermo Fisher Scientific, Catalog No. 165305). The LDH-induced luminescence was measured in a plate reader (EnVision plate reader 2104, Perkin Elmer). For each sample, the luminescence was measured twice. Additionally, for each series of experiments, a calibration curve was obtained according to the manufacturer's protocol to corroborate the accuracy of our measurements. Purified LDH from the rabbit muscle provided by the manufacturer was serially diluted to obtain the standard curve. Luminescence measurements correspond to light relative units (LRUs).

Experimental design and statistical analysis

Simulations of the magnetic and electric fields produced by RF. The distributions of the electric (E) and magnetic (B) fields applied to the cells were simulated using the finite-difference time-domain (FDTD) method implemented by the openEMS project (https://openems.de/start/). Simulations were done considering the 5 cm diameter RF coil or the 2.8 cm diameter RF coil containing a recording chamber filled with imaging saline solution. The saline solution was geometrically modeled to reflect the two-compartment chamber used for Ephys recordings, and the relative permittivity and conductivity of the saline solution were set to 80 and 1.5 S/m, respectively. Wires for the Ephys setup were modeled as perfect electrical conductors, and the headstage input was modeled as a 500 MΩ resistance. Simulated voltage pulses were injected across the coils, and the resulting time-domain fields and voltages were transformed into frequency-domain fields and voltages. At 180 MHz, all fields and voltages were scaled to give a 1.6 µT magnetic field amplitude at the bottom of the recording chamber center. Given this magnetic field strength, amplitudes for electric fields at 180 MHz at the bottom of the recording chamber center and voltages at 180 MHz across the 500 MΩ headstage resistance were recorded. Cells and more complicated patch-clamp circuitry were not modeled.

Ca^{2+} imaging analysis. Cytosolic Ca^{2+} levels were monitored in cells expressing GCaMP6 and either FeRIC or WT TRPV channels. The fluorescence intensity of GCaMP6 was acquired at 1 Hz. GCaMP6 fluorescence was computed in a cell-based analysis with a customized MATLAB (Release 2018b, MathWorks) code. Maximum intensity projection was performed along the time axis to get the maximum intensity signal of cells expressing GCaMP6 in the field of view. In experiments where cells were stimulated with agonists, the maximum intensity projection corresponds to those cells that expressed functional ion channels. The watershed algorithm (MATLAB implemented function: watershed transform; Meyer, 1994) was used to identify and label the cells to generate a cell-based mask for each experiment. The algorithm does not contain a motion correction component because the spatial movement of the cells during the time-lapse acquisition was negligible. The GCaMP6 fluorescence intensity was measured for each masked cell of the time-lapse acquisition (600 s). The GCaMP6 fluorescence signal is presented as $\Delta F/F_0$, where F_0 is the basal fluorescence averaged over the 1–121 s time interval before the start of stimulation and ΔF is the change in fluorescence with respect to the basal values. For analysis, GCaMP6 fluorescence measurements corresponding to the first five frames were

discarded because of an inconsistent artifact. For each masked cell, the data from 6 to 121 s were fit with a monoexponential curve [$f(t; a, b) = ae^{bt}$]. The fitted curve was used to correct the GCaMP6 photobleaching effect over the entire acquisition period. The masked cells that showed abnormal behavior, observed as the fitted growth factor (b) value above 0.002, were excluded from the analysis. Masked cells were considered responsive when the averaged $\Delta F/F_0$ over the time period from 122 to 601 s (RF stimulation) increased >10 times the standard deviation of the GCaMP6 $\Delta F/F_0$ of the basal session. For each experimental group, the changes in GCaMP6 $\Delta F/F_0$ and the corresponding area under the curve (AUC; $t = 121$–601 s) of all analyzed masked cells, which corresponded to all TRPV-expressing cells, were averaged. The plots of the GCaMP6 $\Delta F/F_0$ changes correspond to the data obtained from all identified cells, including both responsive and nonresponsive cells. The MATLAB code that we used for the Ca^{2+} imaging analysis is available in the Data and Materials Availability section.

Nonstationary noise analysis—estimation of unitary current and conductance. The nonstationary noise analysis of macroscopic currents allows us to estimate diverse ion channels' properties such as the unitary current (i). This analysis uses the relationship between the mean current amplitude (I) and the variance of the current (σ^2) given by $\left[\sigma^2(I) = iI - \frac{I^2}{N} + \sigma_b^2\right]$. In this expression, N is the estimated number of channels and σ_b^2 is the background noise (Sigworth, 1980; Traynelis and Jaramillo, 1998; Alvarez et al., 2002; Lingle, 2006; Hartveit and Veruki, 2007). A parabola is fitted to the experimental data where the open-channel probability (P_o) ranges from 0 to 1, but for P_o values smaller than 0.2, only the parabola roots are observed. The slope in the neighborhood of either root of the parabola corresponds to i. For each inward current, the mean I amplitude and σ^2 were measured. Next, the I and σ^2 values were used to obtain the I–σ^2 relationship. In our conditions, we observed only one parabola root (Fig. 1*E*), which was used to estimate i. The i value was used to estimate the conductance (γ) of $TRPV4^{FeRIC}$ using the relationship given by $\left[\gamma = \frac{i}{V}\right]$, where V is the driving force that corresponds to the difference between the V_h (−60 mV) and the theoretical reversal potential for TRPV4 (5 mV).

Voltage imaging analysis—BeRST 1: fast depolarization events/spiking rate inference. The slow imaging rate of the camera system used to observe the BeRST 1 fluorescence changes renders resolving single AP firing challenging and difficult. The imaging system integrates BeRST 1 fluorescence signals over the sampling interval of 21.5 ms. Because the observed BeRST 1 fluorescence signal is the result of fired APs convolved with an unknown BeRST 1 fluorescence signal integration kernel, the state-of-the-art deconvolution algorithm can be employed to infer the precise location of the APs underlying the integrated BeRST 1 time series data. We exploit an extension of the fast nonnegative deconvolution (FOOPSI) method (Vogelstein et al., 2010). The constrained deconvolution approach permits the estimation of the general autoregressive time constants of varying orders, which allows the calculation of the transfer function that characterizes the transformation from neuronal spikes to the integrated BeRST 1 fluorescence change data (Pnevmatikakis et al., 2016). Implementation of this constrained FOOPSI algorithm is found inside the deconvolution package of CaImAn, an open-source calcium imaging data analysis tool (Giovannucci et al., 2019). The constrained FOOPSI algorithm solves a convex optimization inverse problem with a sparsity prior assumption in the forward convolution model. The forward model of the algorithm assumes that the occurrences of spikes are sparse in time, which can be safely assumed. BeRST 1 $\Delta F/F_0$ data with the low-frequency drift component removed was inputted into the algorithm with a custom noise standard deviation parameter and a custom baseline fluorescence value computed for each cell in every experiment. All other constrained FOOPSI algorithm parameters, including the unknown time constants of the kernel, are estimated automatically. The algorithm used CVX (http://cvxr.com/cvx/), a package used to solve convex programs (Grant and Boyd, 2008).

The noise standard deviation parameter was computed for each BeRST 1 $\Delta F/F_0$ recording. For every neuron, the time series component corresponding to the basal activity was computed using a moving standard deviation of length 23 samples, which equates to ∼500 ms in time. The basal activity time series was taken to be the 23-sample-long vector that had the standard deviation equal to the median of the bottom 25th percentile range of moving standard deviations. This process allowed us to automatically select the temporal range in the data corresponding to no observed spiking activity. The remaining components of the time series were taken to be the nonbasal activity time series. The noise standard deviation and the baseline fluorescence value parameters were set to the standard deviation and mean of this estimated basal activity component for each cell, respectively.

The constrained FOOPSI algorithm outputs inferred spikes of varying strengths given the above BeRST 1 $\Delta F/F_0$ data input and the noise standard deviation and baseline fluorescence value input parameters. Because the inferred spikes of small amplitudes are often extraneous and artifacts of deconvolution, we developed a custom-filtering routine to separate the most probable spikes from noise. In recordings where noticeable spikes were present, i.e., time series data where the percent change from the basal activity standard deviation to the nonbasal activity standard deviation exceeded 75%, only inferred spikes with amplitudes greater than the custom threshold of the baseline fluorescence value plus 1.5 times the noise standard deviation were registered as components of the final inferred depolarization events. In order to mitigate extraneous, noisy spike events from biasing our inference of depolarization events, we increased this threshold to be the baseline fluorescence value plus four times the noise standard deviation in recordings where there did not exist noticeable spikes in the BeRST 1 fluorescence data. This filtering algorithm pipeline, which is a slight modification of the thresholded FOOPSI algorithm, removes multiple false-positive spikes and yields accurate and reliable inference of spikes hidden under the integrated BeRST 1 fluorescence change data (Friedrich et al., 2017).

Statistical analyses. For all experimental groups, at least three independent experiments were conducted. Differences in continuous data sets were analyzed using Microcal OriginPro 2021 9.8 software (OriginLab). Data are means ± SEM. When only two experimental groups were compared, the statistical probe applied was the Student's t test. For comparisons of repeated measurements (basal, RF, post-RF), the two-tailed Student's t test probe was applied. For results with normal distributions, hypothesis testing was performed using a one-way ANOVA, followed by Bonferroni's multiple comparisons test. For results that did not follow a normal distribution, hypothesis testing was performed using a nonparametric one-way Kruskal–Wallis ANOVA, followed by Dunn's multiple comparisons test. To compare results according to the levels of two categorical variables, we used a two-way ANOVA, followed by the Holm–Sidak multiple comparisons test. To test if the proportions of spiking versus nonspiking neurons under RF and no RF conditions were significantly different from each other, we employed Fisher's exact test, which uses a contingency table. The contingency table comprised two groups (Group 1, no RF; Group 2, RF), and a binary variable delineated whether or not a neuron was spiking (spiking was assigned a value of 1 and nonspiking was assigned a value of 0). Where applicable, $*p < 0.05$, $**p < 0.001$, or $***p < 0.0001$ was considered a statistically significant difference.

The onset of RF-induced depolarization or hyperpolarization was detected when the membrane potential exceeded the standard error of the basal value for a minimum of 1 min. The membrane potential was monitored during the 5 min stimulation period and continued into the subsequent 5 min post-RF period. The recovery period was estimated to be the time period when the membrane potential returned to a value within the standard error of the basal value after RF was turned off.

Results

Simultaneous RF stimulation and Ephys recordings with minimal electromagnetic interference

In magnetogenetics, the most commonly used RF stimulus frequencies range from ∼300 kHz to 180 MHz. Initially, we expected low electromagnetic interference because those RF frequencies are several orders of magnitude higher than those

utilized in the Ephys setup, which is low-pass-filtered with the cutoff frequency set at 3 kHz. However, when implemented, RF magnetic fields coupled to the Ephys setup produced electric fields on the wires and RF voltages on the patch-clamp headstage. The amplitudes of the electric fields and RF voltages are proportional to the rate of change of the magnetic flux through the loop(s) formed by the various Ephys circuit elements (wires, electrodes, cell bath, etc.). Via nonlinearities in the circuit elements, the RF-induced voltages appear as baseline shifts (Fig. 1*A*). Implementing the Ephys setup with an RF coil measuring 5 cm in diameter delivering 6 µT RF at 180 MHz produced a baseline shift of the measured current from a pipette in-the-bath of >4,400 pA (Fig. 1*A*,*a*). This RF-induced baseline shift hampers performing patch-clamp experiments. To reduce the magnetic flux, a custom-built RF-emitting coil (2.8 cm in diameter) was attached to the bottom of the recording chamber (Fig. 1*D*). The small RF coil allowed focused delivery of the RF stimulus (Fig. 1*B*) and decreased the electrical interference transmitted to the patch-clamp electrode by up to 50% compared with the 5 cm diameter coil. To further decrease the RF interference, two ferrite beads designed to block frequencies near 180 MHz were placed over the cables connected to the RF coil (Fig. 1*C*). The ferrite beads prevented unwanted RF radiation from the cables and drastically reduced the baseline current shift under RF stimulation using either the 5 or 2.8 cm diameter RF coils (Fig. 1*A*,*b*–*d*). We found that combining the 2.8 cm diameter RF coil with the ferrite beads and decreasing the 180 MHz RF stimulus amplitude to 1.6 µT yielded a minimal RF-induced baseline shift (Fig. 1*A*,*d*). Next, to better assess the interference of RF in the patch-clamp headstage, using the ferrite beads, we measured the basal shift in the current and the voltage of a pipette in-the-bath produced by RF at 180 MHz ranging in strength from 0.2 to 10 µT in voltage-clamp ($V_h = 0$ mV) and current-clamp (holding current = 0 pA) configurations (Fig. 2*A*,*B*). The baseline shifts in both configurations, as a function of the RF magnetic field amplitude, are fit with a quadratic term because DC terms are expected to vary with the square of the RF voltage, and the coefficient of the quadratic term is expected to be dependent on the properties of the headstage (Analog Devices Inc., 1993). In voltage-clamp configuration, the RF-induced baseline shift was ~0.4–1.4 pA for RF amplitudes from 1 to 2 µT, but it robustly increased at larger RF amplitudes (Fig. 2*A*). Similar effects were observed when the shifts were measured in the current-clamp configuration (Fig. 2*B*). We then compared the interference levels observed in the patch-clamp setup at three distinct RF frequencies: 345 kHz, 465 kHz, and 180 MHz. The kHz RF frequencies have been used by other groups to activate ferritin-coupled TRPV1 channels (Stanley et al., 2015, 2016; Brier et al., 2020; Mundell et al., 2024). To measure the baseline shift as a function of the RF voltage in a repeatable manner, we used a waveform generator capacitively coupled (Fig. 2*C*, inset) or directly connected (Fig. 2*D*, inset) to the patch-clamp headstage. For low RF voltages, the baseline shifts (nA) in the voltage-clamp configuration as a function of RF voltage are fit with a one-term quadratic polynomial (Fig. 2*C*,*E*, insets). As the RF voltage and corresponding baseline shifts increase, higher-order nonlinearities dominate over the initial second-order nonlinearity, making the baseline shifts increase faster. Remarkably, RF at 345 and 465 kHz saturates the patch-clamp amplifier at a voltage over an order of magnitude less than that of 180 MHz RF; for small RF voltages, the coefficient of the quadratic fit is orders of magnitude larger for 345 and 465 kHz than 180 MHz

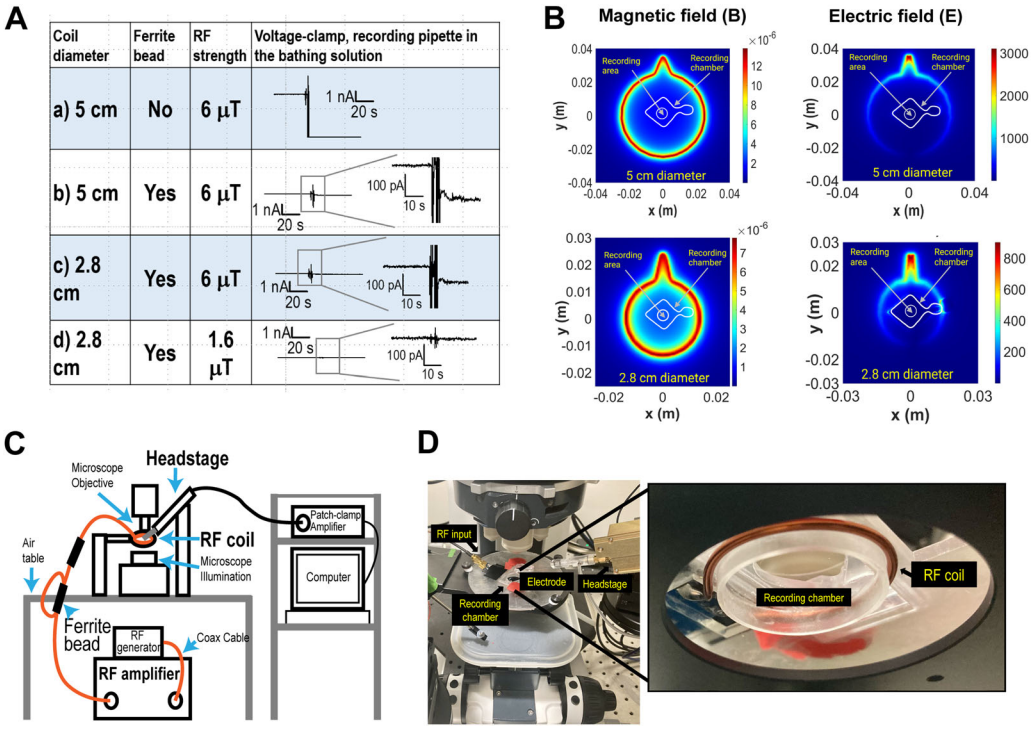

Figure 1. RF-induced electromagnetic interference in the patch-clamp setup. ***A***, Shifts of the baseline current recorded from a pipette in-the-bath (6.9 MΩ) in the voltage-clamp configuration (0 mV). For each RF condition, the RF-emitting coil diameter, the use of ferrite beads, and the RF amplitude are indicated. ***B***, FDTD electromagnetic simulation for an RF coil measuring 5 or 2.8 cm in diameter. Magnitudes of (left) 180 MHz magnetic and (right) electric fields are shown with all fields scaled for a magnetic field with an amplitude of 1.6 µT at the center. The amplitudes of the electric fields at the center were 13.1 and 5 V/m for the 5 and 2.8 cm diameter RF coils, respectively. ***C,D***, Illustration and pictures of the Ephys setup and RF system used for patch-clamp recordings of cells stimulated with RF. (***D***, right) A custom-built 2.8 cm diameter RF-emitting coil (180 MHz) was attached to the bottom of the recording chamber.

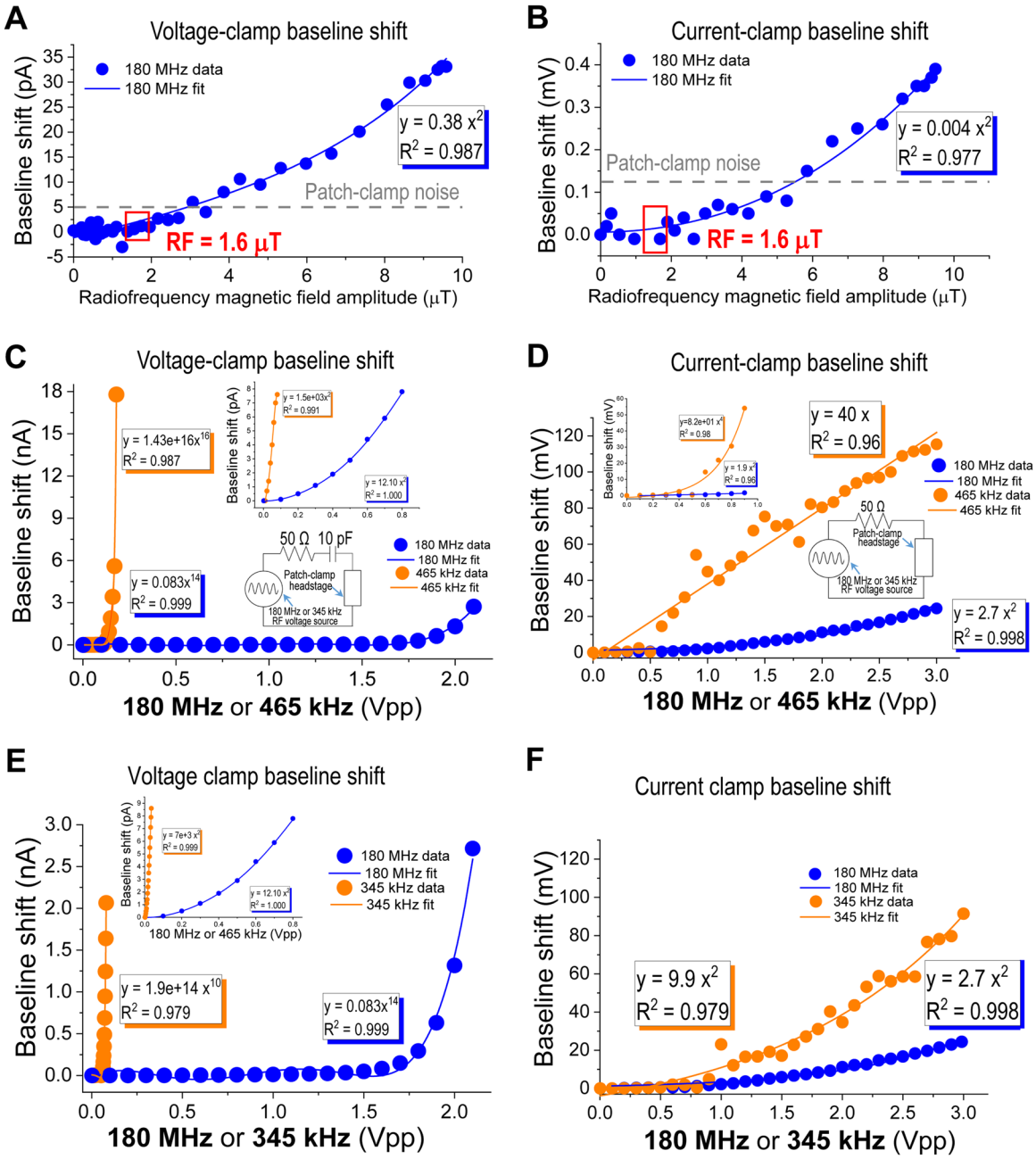

Figure 2. RF-induced baseline shift in patch-clamp recordings. ***A,B***, The baseline shift recorded from a pipette in-the-bath (8 MΩ) is shown for the (***A***) voltage-clamp or (***B***) current-clamp configuration as a function of the 180 MHz RF amplitude in microtesla. The data fits (solid lines) and the equations are indicated. ***C,D***, The baseline current shift is shown for the (***C***) voltage-clamp (inset, zoom in) or (***D***) current-clamp configuration as a function of RF voltage on the voltage source from the RF generator at 180 MHz (blue) or 465 kHz (orange). The data fits (solid lines) and the equations are indicated. Insets: Illustrations of the setups used to measure the baseline shifts produced by an RF source at 180 MHz or 465 kHz. ***E,F***, The baseline current shift is shown for the (***E***) voltage-clamp (inset, zoom in) or (***F***) current-clamp configuration as a function of RF voltage on the voltage source from the RF generator at 180 MHz (blue) or 345 kHz (orange). The data fits (solid lines) and the corresponding equations are indicated.

(Fig. 2*C*,*E*, insets). The baseline shifts (mV) in the current-clamp configuration as a function of RF voltage are fit with various one-term polynomials, and the baseline shift from 465 kHz is observed to increase much faster than that from 180 MHz (Fig. 1*D*). However, compared with the voltage-clamp configuration, the difference is not as significant, and the voltage at which they become significantly different is higher (Fig. 1*D*). For RF at 345 kHz, data are fit with quadratic terms having a higher coefficient relative to 180 MHz (Fig. 1*F*). These results emphasize the need to keep RF voltages induced on the headstage low and highlight the fact that RF at 345 and 465 kHz produces larger baseline shifts compared with RF at 180 MHz. Therefore, as in our previous studies, we conducted all experiments using RF at 180 MHz. For patch-clamp recordings, we selected an RF amplitude of 1.6 µT because it does not produce a significant basal shift relative to the intrinsic noise of the patch-clamp measurements and because it is sufficient to activate FeRIC channels.

RF depolarizes neurons expressing TRPV4^{FeRIC} and increases their spiking activity

To validate ferritin-based magnetogenetics as a tool to control neurons, we conducted Ephys recordings and voltage imaging

experiments. We utilized cultured hippocampal neurons that were transfected with a bicistronic vector, which allows simultaneous expressions of $TRPV4^{FeRIC}$ and the fluorescent reporter mCherry. The RF stimulus (180 MHz and 1.6 μT) was delivered using the 2.8 cm diameter coil, and ferrite beads were included in the Ephys setup. To prevent error due to any RF-induced basal shift, we measured the bioelectrical properties of neurons at three time points: before RF (baseline), during (RF), and within 2 min after RF stimulation (post-RF). We expected the effects of RF to be detectable within a few minutes because we previously observed a gradual and sustained activation of $TRPV4^{FeRIC}$ by RF, leading to increases in cytosolic Ca^{2+} levels over minutes (Hernández-Morales et al., 2020, 2021). Utilizing N2a cells expressing $TRPV4^{FeRIC}$, we verified that RF stimulation induces concurrent inward currents and cytosolic Ca^{2+} increases that persist for a few minutes poststimulation (Fig. 3*A–C*). To test the effects of RF on neurons, we first verified that the expression of $TRPV4^{FeRIC}$ does not affect the basal passive and active electrical properties of neurons. Using the current-clamp configuration, we observed that the I–V relationship and the number and amplitude of APs were similar in mock-transfected neurons ($n = 8$ cells) and neurons expressing $TRPV4^{FeRIC}$ ($n = 11$; Fig. 3*D–F*). Next, using the voltage-clamp configuration, we examined the RF effects of the neuronal membrane potential (Fig. 3*G*). RF did not affect the membrane potential of mock-transfected neurons (basal, −59.9 ± 1.8 mV; post-RF, −60.1 ± 2.1 mV; $p = 0.78$; $n = 5$ cells; Fig. 4*A*) or neurons expressing $TRPV4^{WT}$ channels (basal, −54.7 ± 2.3 mV; post-RF, −53.5 ± 3 mV; $p = 0.32$; $n = 8$ cells; Fig. 4*B*). However, in neurons expressing $TRPV4^{FeRIC}$, RF gradually depolarized the membrane potential (basal, −58.8 ± 1.8 mV; post-RF, −57.1 ± 1.4 mV; $p < 0.05$; $n = 9$ cells; Fig. 4*C*). The onset of the depolarizing RF effect was highly variable, ranging from 1 to 8 min (4.4 ± 1.3 min; $n = 9$). The onset of the RF effect was defined as the time when the membrane potential remained depolarized above the standard error of the basal potential for at least 1 min. The recovery of the membrane potential to basal levels was also highly variable and was observed in ∼44% of the neurons when examined within the 5 min period following RF stimulation. The TRPV4 antagonist GSK 2193874 (GSK219, 1 μM) inhibited the RF-induced membrane depolarization (baseline, −59.14 ± 1.68 mV; post-RF, −58.65 ± 0.86 mV; $p = 0.66$; $n = 8$ cells; Fig. 4*E*). In this series of experiments, neurons were preincubated with GSK219 for at least 20 min before RF stimulation. Similarly, the antioxidant Trolox (100 μM) inhibited the RF effect on the membrane potential of neurons expressing $TRPV4^{FeRIC}$ (basal, −62.84 ± 1.39 mV; post-RF, −63.21 ± 1.11 mV; $p = 0.81$; $n = 7$ cells; Fig. 4*F*). The Trolox findings corroborate that, similar to our previous observations in N2a cells (Hernández-Morales et al., 2020), RF stimulation triggers the activation of $TRPV4^{FeRIC}$ in neurons through a ferritin-dependent mechanism involving the generation of endogenous ROS and oxidized lipids. Subsequently, we investigated the effects of arachidonic acid (AA) in neurons expressing $TRPV4^{FeRIC}$. AA was chosen for comparison with RF effects due to our previous observation of RF causing an ∼2.5-fold increase in AA levels in N2a cells expressing $TRPV4^{FeRIC}$ (Hernández-Morales et al., 2020). The application of AA (20 μM) to $TRPV4^{FeRIC}$-expressing neurons resulted in membrane depolarization (basal: −62.57 ± 1.57 mV; AA, −57.39 ± 2.76 mV; $p = 0.03$; $n = 7$ cells; Fig. 4*D*) with kinetics closely resembling those produced by RF stimulation (refer to Fig. 4*C*). In addition, we monitored the Rm of neurons by applying a 5 pA square current pulse every 30 s. The Rm value is influenced by the activity and conductance of the ion channels. A decrease in Rm indicates an increase in the number of open ion channels or conductance at the cell membrane, while an increase in Rm suggests a reduction in the activity of the membrane ion channel. In neurons expressing $TRPV4^{FeRIC}$, RF decreased the Rm with respect to the basal level (80 ± 10%; $n = 7$ cells; $p < 0.05$) but did not change the Rm in neurons treated with GSK219 (103 ± 9%; $n = 8$ cells). Likewise, RF did not change the Rm in mock-transfected neurons (101 ± 6%; $n = 5$ cells) or neurons expressing $TRPV4^{WT}$ (104 ± 16%; $n = 8$ cells). These results indicate that RF activates $TRPV4^{FeRIC}$ leading to membrane depolarization. Our results and previous studies (Brier et al., 2020; Hernández-Morales et al., 2020; Mundell et al., 2024) have demonstrated that RF interaction with ferritin generates ROS, which are responsible for TRPV4 activation. Interestingly, contrary to our initial expectations, we did not observe any discernible RF-induced triggering of APs. Likewise, when applying AA directly to neurons expressing $TRPV4^{FeRIC}$, the membrane was depolarized, but no APs were elicited. This suggests that the activation of these channels with endogenous lipids and oxidized lipids is insufficient per se to reach the AP threshold. Remarkably, the RF-induced membrane depolarization persisted for several minutes following stimulus cessation. This phenomenon indicates that the ROS generated by RF may not be promptly neutralized in these neurons, sustaining their effects on $TRPV4^{FeRIC}$ channels beyond the stimulus period. The RF-induced membrane depolarization, albeit of subthreshold amplitude, has the potential to influence neuronal excitability. The RF-induced depolarization increases the likelihood of a neuron reaching the threshold to fire APs, making them more responsive to excitatory inputs. We tested this hypothesis by conducting voltage imaging experiments with the voltage-sensitive fluorophore BeRST 1 (Huang et al., 2015; Walker et al., 2021), which allows the examination of spiking frequency in a large number of neurons. Hippocampal neurons expressing either $TRPV4^{FeRIC}$ or the WT TRPV4 ($TRPV4^{WT}$) were labeled with BeRST 1 (500 nM) and imaged at 46.5 Hz (Fig. 4*G,H*). We developed a custom algorithm tailored to inferring the spiking frequency from the time series data of BeRST 1 fluorescence changes (see Materials and Methods). Although we were not able to distinguish between APs, Ca^{2+} spikes, or postsynaptic potentials, voltage imaging led to consistent observations of the neuronal spiking activity (Fig. 5*A*). The reported BeRST 1 data are the average spiking frequency (Hz ± SEM) from both spiking and nonspiking neurons. To observe the intrinsic activity, neurons were imaged with no added neurotransmitter receptor antagonists or ion channel blockers. Neurons were imaged in the absence and presence of RF stimulation (Fig. 4*H*). In $TRPV4^{FeRIC}$-expressing neurons (mCherry positive), RF stimulation significantly increased the spiking frequency compared with that of mock-transfected neurons (Figs. 4*H,I*, 5*C*; mock-transfected + RF: 0.006 ± 0.002 Hz, $n = 181$ cells; $TRPV4^{FeRIC}$ + no RF: 0.13 ± 0.06 Hz, $n = 90$ cells; $TRPV4^{FeRIC}$ + RF: 0.34 ± 0.09 Hz, $n = 94$ cells; $p < 0.05$). Additionally, RF also increased the percent of spiking neurons (no RF: 17%, $n = 90$ cells; RF: 39%, $n = 94$ cells; Fig. 5*B*), defined as $TRPV4^{FeRIC}$-expressing mCherry-positive neurons displaying at least one spike in the entire experiment. RF effects were abolished with the TRPV4 antagonist GSK219 (0.03 ± 0.02 Hz; $n = 24$ cells; $p = 0.08$; Fig. 4*I*). These results indicate that RF activates $TRPV4^{FeRIC}$ channels increasing the neurons' spiking

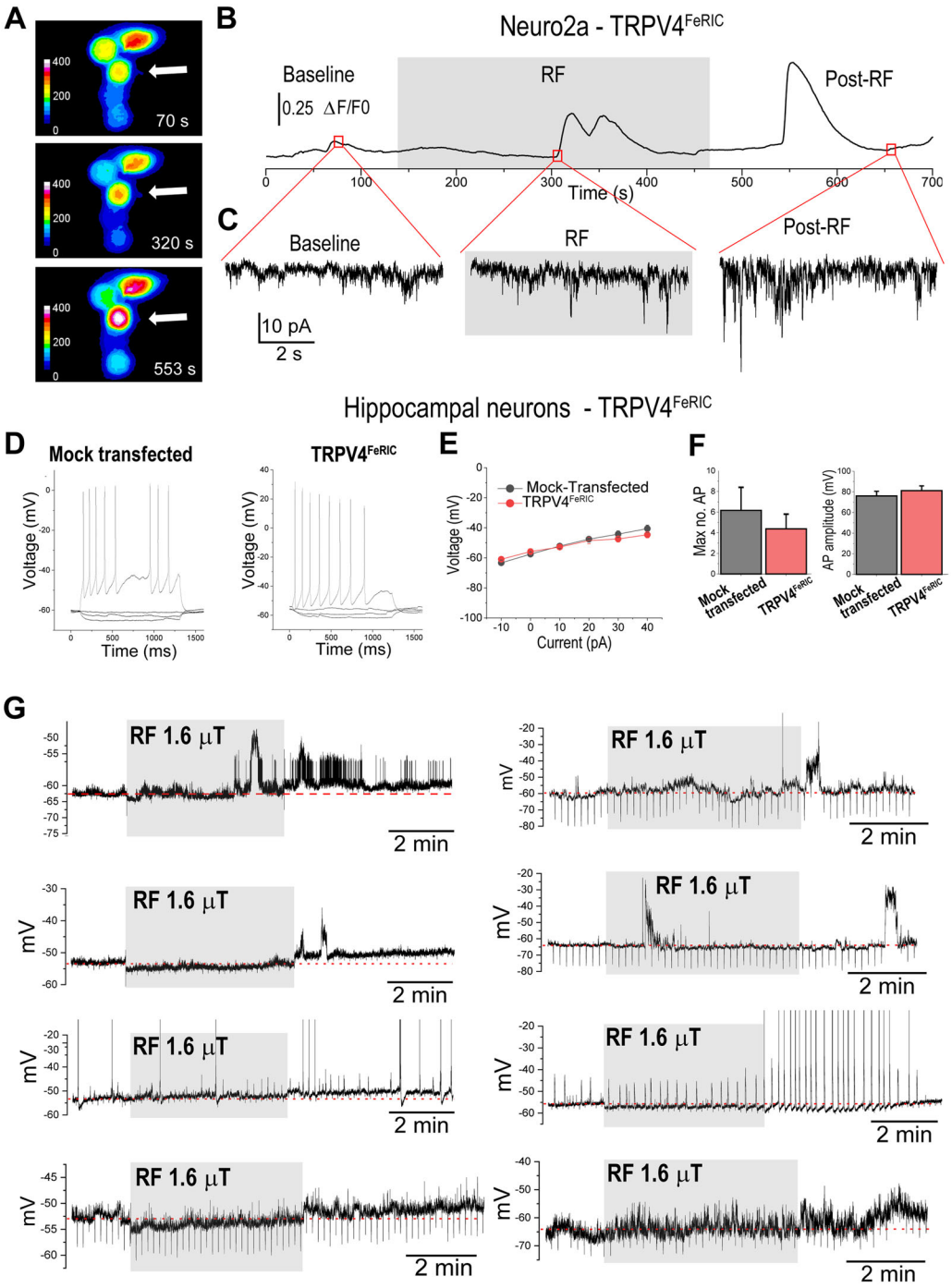

Figure 3. RF evokes Ca^{2+} transients and controls the bioelectrical properties of Neuro2a and hippocampal neurons expressing $TRPV4^{FeRIC}$. ***A***, Pseudocolor images of GCaMP6 fluorescence from N2a cells expressing $TRPV4^{FeRIC}$ before (70 s), during (320 s), and after RF stimulation (553 s). The white arrow indicates a patch-clamped N2a cell that was responsive to RF stimulation. ***B***, Changes in GCaMP6 fluorescence and (***C***) membrane currents from the cell in (***A***) before (baseline), during (gray box), and after RF (post-RF) stimulation. ***D***, Voltages and APs generated by square current pulses (starting at −10 pA with 10 pA increases) applied to neurons recorded in the whole-cell current-clamp configuration. Mock-transfected neurons (left) and neurons expressing $TMEM16A^{FeRIC}$ (right). ***E***, Current–voltage relations in mock-transfected neurons ($n = 8$ cells) and neurons expressing $TRPV4^{FeRIC}$ ($n = 11$ cells). ***F***, Average (±SEM) of active neuronal properties of mock-transfected neurons ($n = 8$ cells) and neurons expressing $TRPV4^{FeRIC}$ ($n = 11$ cells). No statistically significant difference was found when comparing the experimental groups (two-tailed Student's *t* test). ***G***, Representative traces of membrane voltages recorded from $TRPV4^{FeRIC}$-expressing neurons in the current-clamp configuration before, during, and after RF stimulation (gray square). The dotted red line indicates the level of the basal membrane potential. In some traces, downward vertical lines correspond to the membrane voltage changes induced by the 5 pA square pulse applied to measure the Rm. In some recordings, neurons displayed APs, observed as upward vertical lines.

frequency. On the contrary, in neurons expressing $TRPV4^{WT}$, RF did not change the spiking frequency (Figs. 4*I*, 5*D*; no RF: 0.015 ± 0.02 Hz, $n = 13$ cells; RF: 0.02 ± 0.01 Hz; $n = 15$ cells). We observed an increase in the percent of spiking neurons expressing $TRPV4^{WT}$ following RF stimulation (no RF: 8%, $n = 13$ cells; RF: 33%, $n = 15$ cells; Fig. 5*B*), but it was not statistically significant. The collective Ephys and voltage imaging findings suggest that RF activates $TRPV4^{FeRIC}$, producing neuronal membrane depolarization and increasing the spiking frequency. The absence of RF effects on mock-transfected neurons

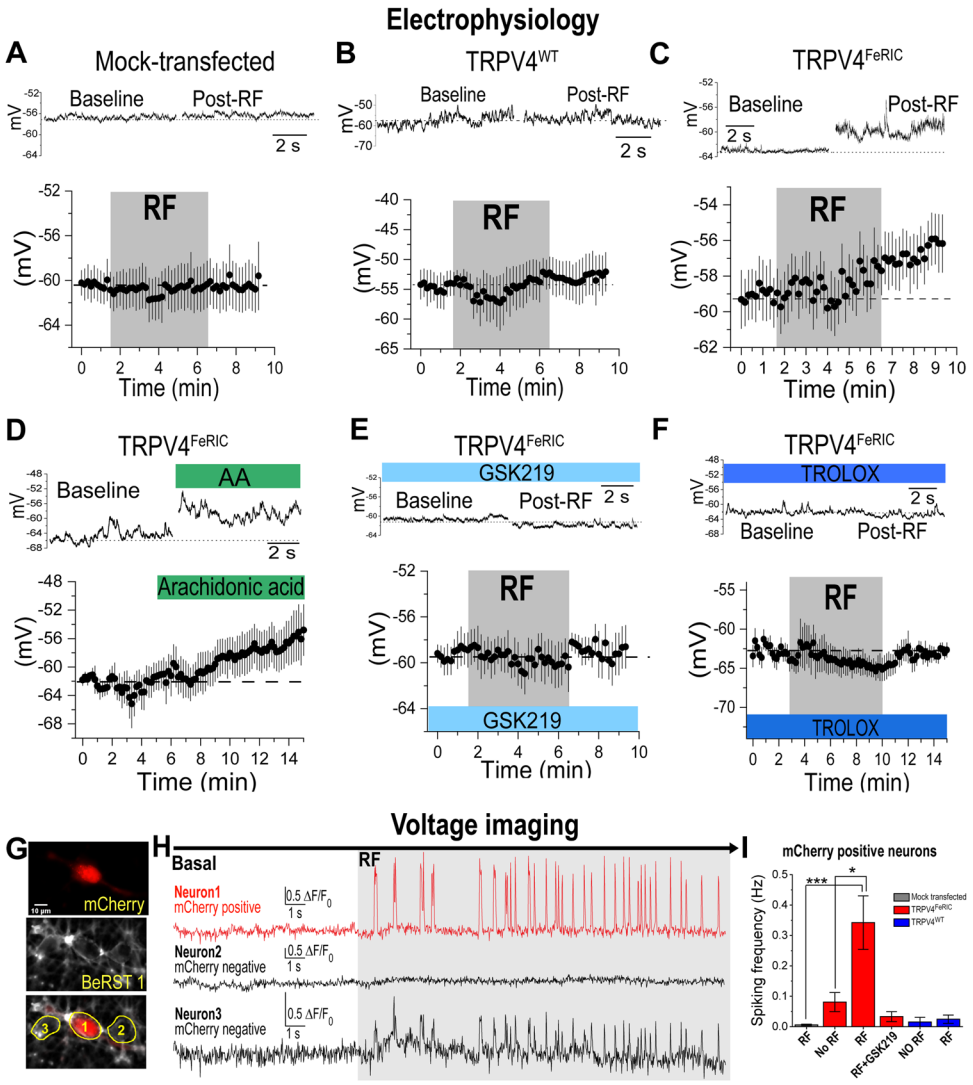

Figure 4. RF depolarizes the membrane potential and increases the spiking frequency in neurons expressing TRPV4^{FeRIC}. ***A–E***, Membrane voltages recorded from neurons in the current-clamp configuration. Representative traces (top) and the average membrane potential (±SEM, bottom) before (baseline) and following RF (post-RF) or AA (20 μM) stimulation in (***A***) mock-transfected neurons ($n = 5$ cells) or neurons expressing (***B***) TRPV4^{WT} ($n = 8$ cells) or (***C–F***) TRPV4^{FeRIC}. For neurons expressing TRPV4^{FeRIC} stimulated with RF, the number of independent experiments is $n = 9$ cells, and for those stimulated with AA, $n = 7$ cells. In separate series of experiments, neurons were treated with (***E***) GSK219 (1 μM, TRPV4 antagonist, $n = 8$ cells) or (***F***) Trolox (100 μM, an antioxidant, $n = 7$) ∼20 min before RF stimulation. ***G***, Epifluorescence images of neurons expressing TRPV4^{FeRIC} (mCherry positive) stained with BeRST 1. ***H***, Changes in BeRST 1 fluorescence in one mCherry-positive neuron (1) and mCherry-negative neighboring neurons (2, 3) from (***G***) before (basal) and during RF stimulation (gray box). ***I***, Averages (±SEM) of spiking frequency (Hz) for total mCherry-positive neurons (spiking and nonspiking). The total number of independent experiments indicated with the letter "*N*" and the total number of cells indicated with letter "*n*" for mock-T-RF is $N = 11$ and $n = 181$ cells, while for mCherry-positive neurons is FeRIC-no RF, $N = 54$, $n = 90$ cells; FeRIC-RF, $N = 38$, $n = 94$ cells; FeRIC-RF-GSK219, $N = 22$, $n = 24$ cells; WT-no RF, $N = 12$, $n = 13$ cells; and WT-RF, $N = 11$, $n = 15$ cells. Experimental groups are independent samples. For patch-clamp results, significance was determined using a two-tailed Student's *t* test. For BeRST 1 results, significance was determined using a Kruskal–Wallis ANOVA followed by Dunn's multiple comparisons test. Where applicable, either $*p < 0.05$ or $***p < 0.0001$ was considered a statistically significant difference.

or those expressing the WT TRPV4 channels suggests that RF specifically acts on TRPV4^{FeRIC}-expressing neurons.

RF hyperpolarizes and inhibits neurons expressing TMEM16A^{FeRIC}

In the adult central nervous system, inhibitory transmission is mediated primarily by chloride (Cl^-) currents through diverse ligand-gated ionotropic receptors such as GABA and glycine receptors. To achieve neuronal inhibition using FeRIC, we required a chloride-permeable ion channel sensitive to ROS and oxidized lipids because those are the stimuli generated by the interaction between RF and ferritin (Brier et al., 2020; Hernández-Morales et al., 2020). We selected anoctamin 1, also known as the TMEM16A channel, which is activated by a diverse set of physical and chemical stimuli including ROS, lipids, and lipid peroxidation products (Schreiber et al., 2018, 2019; Dulin, 2020). To couple TMEM16A with endogenous ferritin, it was fused with the ferritin binding D5 of kininogen at the N terminal, referred to as TMEM16A^{FeRIC}. The final construct is a bicistronic vector, which allows simultaneous, but independent, expression of TMEM16A^{FeRIC} and mCherry. Additionally, to examine that D5 does not affect TMEM16A expression at the cell membrane, we generated two TMEM16A^{FeRIC} variants, one is FLAG-tagged (FLAG-TMEM16A^{FeRIC}) and the other is fused with mCherry (TMEM16A^{FeRIC}mCherry). Immunocytochemical assays with an anti-FLAG antibody corroborated the expression of

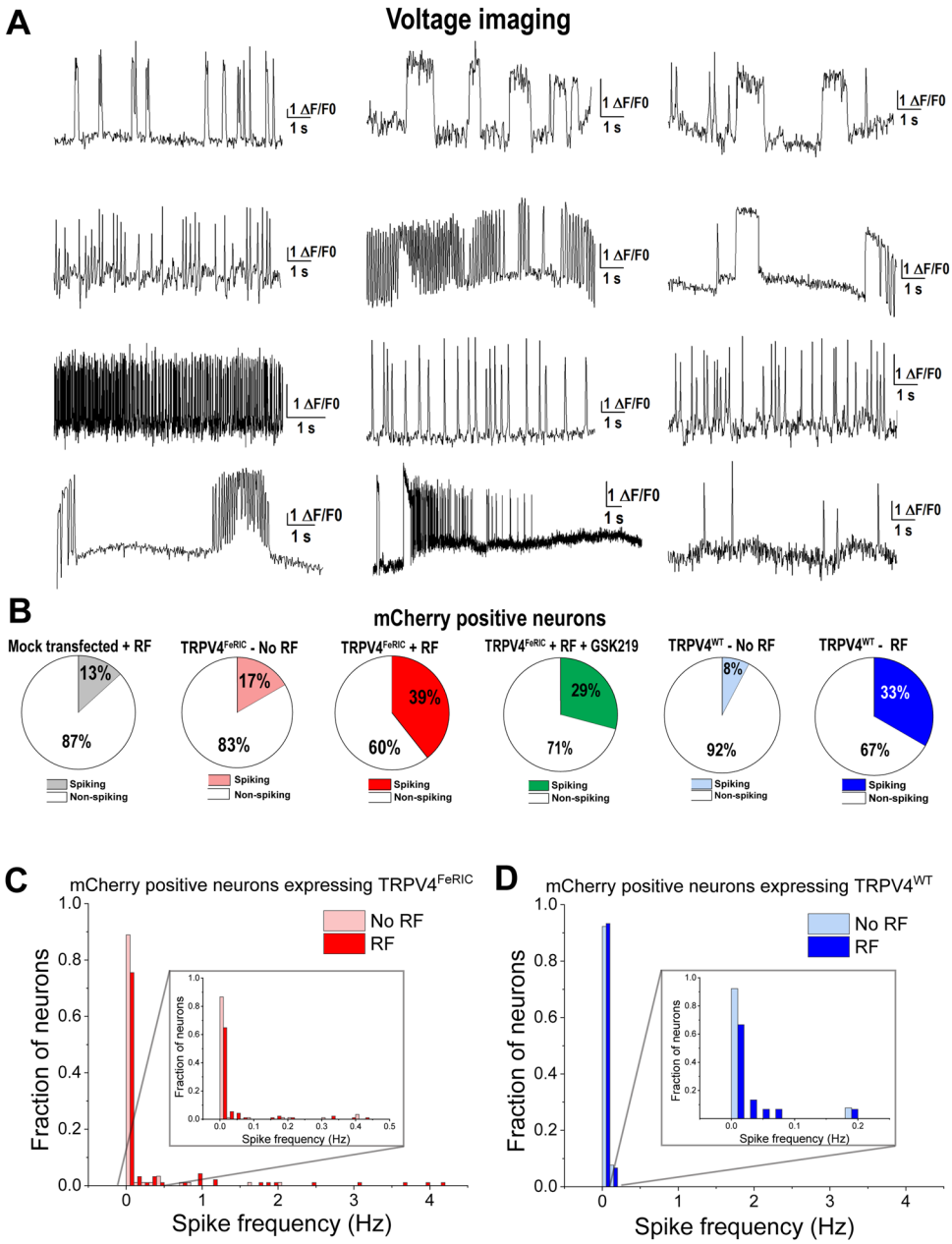

Figure 5. RF affects the spiking properties of hippocampal neurons expressing TRPV4 channels. ***A***, Examples of spiking neurons expressing TRPV4^{FeRIC} upon RF stimulation. ***B***, Pie charts of the fraction of mock-transfected neurons or mCherry-positive neurons expressing FeRIC or WT TRPV4 that were spiking or not spiking before and following RF stimulation. A neuron was considered as spiking if displayed at least one spike over the course of the entire experiment. The number of experiments is FeRIC-no RF, $n = 90$ cells; FeRIC-RF, $n = 94$ cells; FeRIC-RF-GSK219, $n = 24$ cells; WT-no RF, $n = 13$, cells; and WT-RF, $n = 15$ cells. ***C,D***, Histograms show the distribution of the spiking frequencies of neurons expressing (***C***) TRPV4^{FeRIC} or (***D***) TRPV4^{WT} before and following RF stimulation. In neurons expressing FeRIC channels, RF induced a shift of the fraction of neurons displaying higher spiking frequencies ($p = 0.001$). Conversely, in neurons expressing WT channels, RF did not induce a change in neuronal spiking frequency ($p = 0.1727$). Significance was determined using a Fisher's exact test. Where applicable, $p < 0.001$ was considered a statistically significant difference.

TMEM16^{FeRIC} at the cell plasma membrane in N2a cells expressing the channel (Fig. 6*A*). Similarly, using N2a cells, expression of TMEM16A^{FeRIC}mCherry largely colocalized with LCK-GFP, indicating that it is expressed at the cell membrane (Fig. 6*B*). Furthermore, we corroborated that the experimental RF stimulation for 10 min (180 MHz, 10 μT) of N2a cells expressing TMEM16A^{FeRIC} does not affect the cell plasma membrane integrity (Fig. 6*C,D*). Next, we investigated the inhibitory effect of RF in hippocampal neurons expressing TMEM16A^{FeRIC} using patch-clamp recordings, voltage imaging, and Ca^{2+} imaging. We first verified that neurons expressing TMEM16A^{FeRIC} display similar electrical properties compared with mock-transfected neurons. Subsequently, we assessed the effects of RF stimulation on the membrane potential and spontaneous AP activity in neurons expressing TMEM16A^{FeRIC} (Fig. 7*A–C*). In these neurons, RF stimulation (5 min at 180 MHz and 1.6 μT) hyperpolarized the membrane potential with respect to the baseline (baseline, -61.6 ± 2.2 mV; post-RF, -64.1 ± 2.4 mV; $n = 10$ cells; $p < 0.05$; Fig. 7*A–C*). The onset of the hyperpolarizing RF effect was highly variable, ranging from 3 to 9 min (5.8 ± 0.6 min; $n = 10$ cells). The onset of the RF effect was defined as the time when the membrane potential remained hyperpolarized above the standard error of

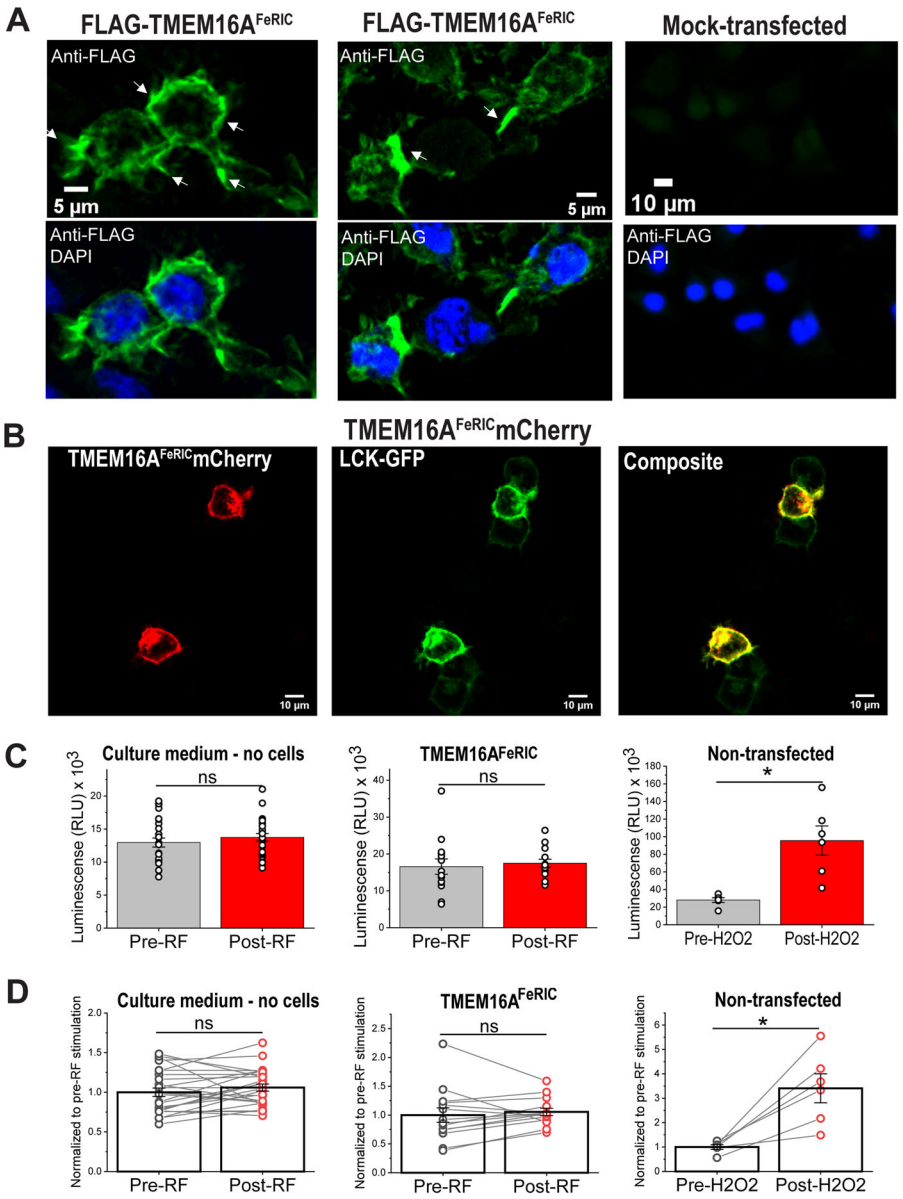

Figure 6. Expression of TMEM16A^{FeRIC} channels in Neuro2a cells. ***A***, Confocal images of Neuro2a cells expressing FLAG-tagged TMEM16A^{FeRIC}. The epitope DYKDDDDK, targeted by the anti-FLAG antibody (green), is utilized for detection. Images of mock-transfected Neuro2a cells labeled with an anti-FLAG antibody, serving as a negative control. Cell nuclei were stained with DAPI (blue). ***B***, Confocal images of living Neuro2a cells coexpressing TMEM16A^{FeRIC} fused with mCherry and the plasma membrane marker LCK-GFP. ***C***, Averages (±SEM) of luminescence LRUs and ***D***, normalized data for LDH bioluminescent detection in the control culture medium ($N = 13$ independent experiments, 2 repeats), nontransfected Neuro2a cells ($N = 3$ independent experiments, 2 repeats), and Neuro2a cells expressing TMEM16A^{FeRIC} channels ($N = 7$ independent experiments, 2 repeats). The LDH assay allows examination of the cytotoxicity effect by quantifying LDH release into the culture medium upon plasma membrane damage. To detect LDH levels, the culture medium was sampled 24 h before and after RF stimulation (180 MHz, 10 µT, 10 min). For positive control, nontransfected cells were treated with 10 µM H_2O_2 for 30 min. Significance was determined using the parametric paired-samples *t* test. Where applicable, $*p < 0.05$ was considered a statistically significant difference.

the basal for at least 1 min. The recovery of the membrane potential to basal levels was also highly variable and was observed in ~40% of the neurons when examined within the 5 min time period following RF stimulation. The RF effect on neurons expressing TMEM16A^{FeRIC} was inhibited by the TMEM16A antagonist Ani 9 (1 µM; Fig. 7*D*,*E*; baseline, −62.7 ± 1.7 mV; post-RF, −62.5 ± 1.7 mV; $n = 12$ cells; $p = 0.43$). Consistently, RF stimulation decreased the frequency of spontaneous APs in TMEM16A^{FeRIC}-expressing neurons (baseline, 0.0258 ± 0.0169 Hz; post-RF, 0.0088 ± 0.0091 Hz; $n = 8$ cells; $p < 0.05$; Fig. 7*F*), but RF did not affect these neurons treated with Ani 9 (baseline, 0.0813 ± 0.0715 Hz; post-RF, 0.0773 ± 0.065 Hz; $n = 5$ cells; $p = 0.65$; Fig. 7*G*). To test the inhibitory effect of RF in a larger number of neurons, we conducted voltage imaging experiments in neurons expressing TMEM16A^{FeRIC} labeled with BeRST 1 and treated with bicuculline (5 µM). Bicuculline is an antagonist of $GABA_A$ receptors, which increases the spiking frequency by blocking the inhibitory GABAergic transmission (Eisenman et al., 2015). Neurons expressing TMEM16A^{FeRIC} treated with bicuculline for 10 min displayed a robust increase in the spiking frequency (0.15 ± 0.07 Hz; $n = 44$ cells) that was drastically decreased by the coapplication of RF (0.002 ± 0.001 Hz; $n = 29$ cells; $p < 0.05$; Fig. 8*A*–*C*). The RF effect on the spiking frequency of TMEM16A^{FeRIC}-expressing neurons was

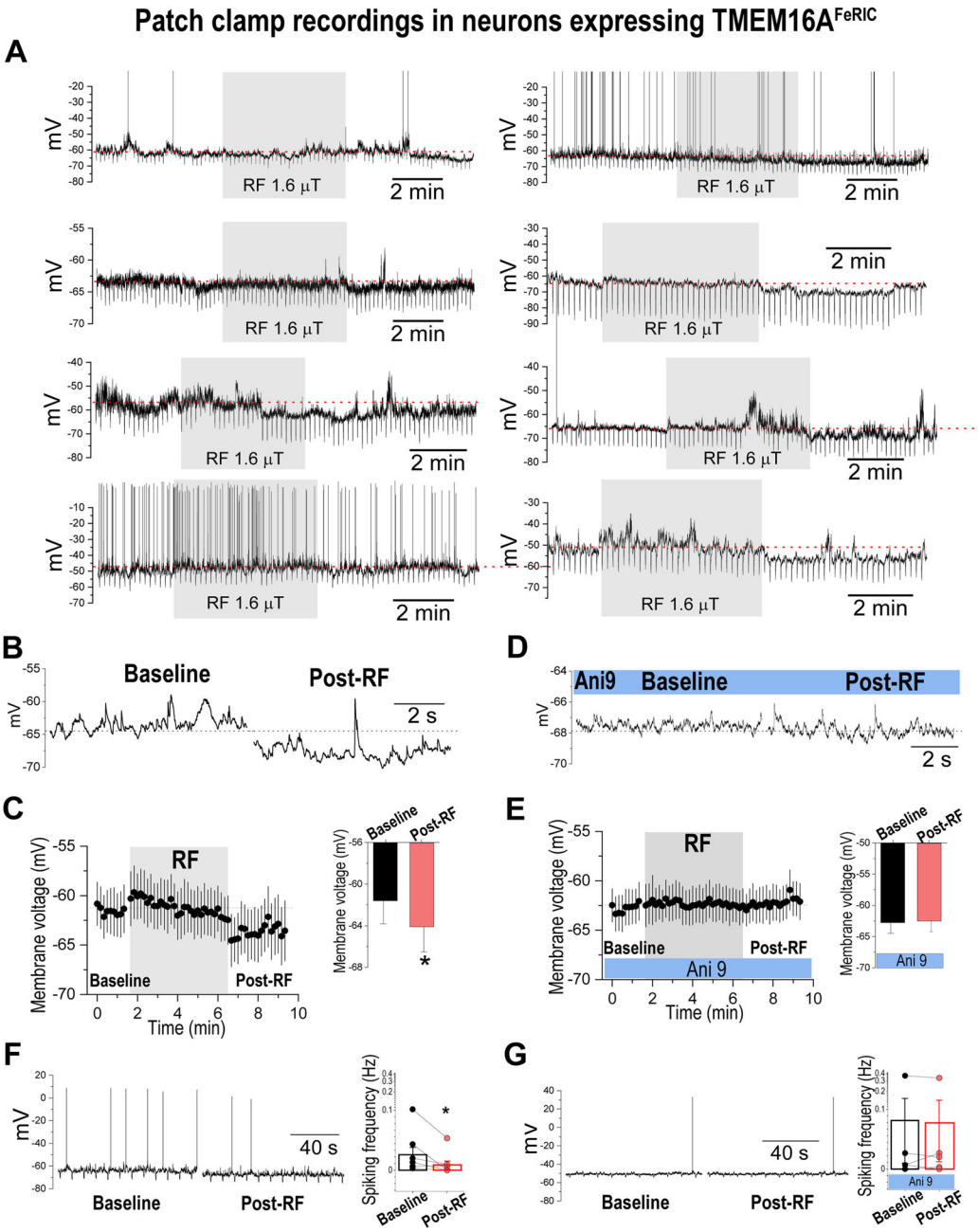

Figure 7. RF hyperpolarizes and inhibits neurons expressing TMEM16A^{FeRIC}. ***A***, Representative traces of membrane voltages recorded from TMEM16A^{FeRIC}-expressing neurons in the current-clamp configuration before, during, and after RF stimulation (gray square). The dotted red line indicates the level of the basal membrane potential. In some traces, downward vertical lines correspond to the membrane voltage changes induced by the 5 pA square pulse applied to measure the Rm. In some recordings, neurons fired APs, observed as upward vertical lines. ***B–E***, Representative traces of the membrane potential and the average membrane potential (±SEM) before RF, during RF, and in the post-RF periods in neurons expressing TMEM16A^{FeRIC} (***B,C***, $n = 10$ cells) in the absence or (***D,E***, $n = 12$ cells) the presence of Ani 9 (1 μM), an antagonist of TMEM16A. Insets: average membrane potential (± SEM) in the baseline and the post-RF period. ***F,G***, Representative spontaneous APs and the average (±SEM) in the baseline and the post-RF periods in neurons expressing TMEM16A^{FeRIC} (***F***, $n = 8$ cells) in the absence or (***G***, $n = 5$ cells) in the presence of Ani 9. Significance was determined using a two-tailed Student's t test. Where applicable, $^*p < 0.05$ was considered a statistically significant difference.

suppressed with Ani 9 (0.28 ± 0.04; $n = 20$ cells; $p < 0.05$; Fig. 8*B,C*). Notably, the increase in the spiking frequency induced by bicuculline was larger in the presence of the antagonist Ani 9 compared with that in its absence. While this suggests a basal activity of the TMEM16A channel, this result does not impact the RF-induced activation of TMEM16A^{FeRIC}. Next, we evaluated whether RF hinders the activation of neurons and the subsequent cytosolic Ca^{2+} transients induced with high extracellular K^+ concentration (70 mM), a strong depolarizing stimulus. In neurons coexpressing GCaMP6 and TMEM16A^{FeRIC}, high K^+ produced robust Ca^{2+} transients (Fig. 8*D,E*). Treating neurons expressing TMEM16A^{FeRIC} with RF for 10 min before applying the high K^+ stimulus produced Ca^{2+} transients with significantly smaller maximum change in the GCaMP6 fluorescence (K^+: 6.8 ± 0.5 $\Delta F/F_0$, $n = 21$ cells; K^+-RF: 4.4 ± 0.5 $\Delta F/F_0$, $n = 38$ cells, $p < 0.05$), but not in the AUC (K^+: 1,503 ± 119, $n = 21$ cells; K^+-RF: 1,061 ± 146, $n = 38$ cells; $p = 0.0593$; Fig. 8*D,E*). The RF effect on the maximum change in GCaMP6 fluorescence was prevented by Ani 9 (max: 7.3 ± 1 $\Delta F/F_0$, $n = 9$ cells, $p < 0.05$; Fig. 7*D,E*). The combined results obtained from the Ephys

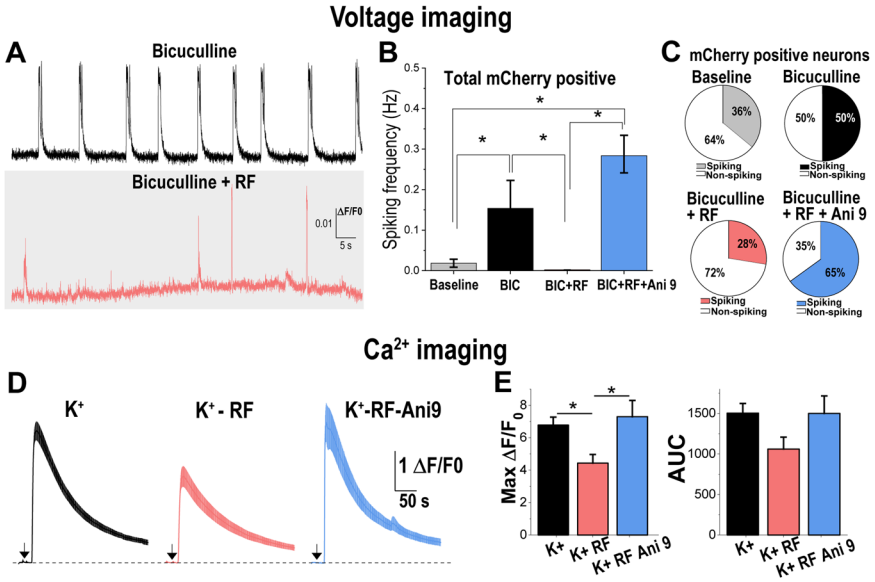

Figure 8. RF inhibits and decreases the spiking frequency in neurons expressing TMEM16A^{FeRIC}. ***A***, Representative changes in BeRST 1 fluorescence in neurons expressing TMEM16A^{FeRIC} following treatment with bicuculline for 10 min in the absence (top) or the presence of RF stimulation (bottom). ***B***, Averages (±SEM) of the spiking frequency (Hz) for mCherry-positive neurons (spiking and nonspiking) for the different experimental groups. Neurons were imaged after treatment with bicuculline for 10 min in the absence ($N = 26$; $n = 44$ cells) or the presence of RF ($N = 25$; $n = 29$ cells) or RF plus Ani 9 ($N = 18$; $n = 20$ cells). ***C***, Pie charts of the fraction of mCherry-positive neurons that were spiking (at least one spike in the entire experiment) or not spiking for the different experimental groups. ***D***, Average changes (±SEM) in GCaMP6 fluorescence in neurons expressing TMEM16A^{FeRIC} following the addition of 70 mM K^+ (black arrow) in non-stimulated (black; $N = 18$; $n = 21$ cells), stimulated with RF (red; $N = 30$; $n = 38$ cells) or stimulated with RF conditions in the presence of Ani 9 (blue; $N = 6$; $n = 9$ cells). ***E***, Bar graphs are the averages (±SEM) of the maximum change in GCaMP6 fluorescence (max. $\Delta F/F_0$) and the AUC of neurons expressing TMEM16A^{FeRIC} for the different experimental groups. Significance was determined using a one-way ANOVA followed by Bonferroni's multiple comparisons test. Where applicable, $^*p < 0.05$ was considered a statistically significant difference.

recordings and the voltage and Ca^{2+} imaging experiments indicate that RF activates TMEM16A^{FeRIC}, inducing membrane hyperpolarization and inhibiting spontaneous and evoked neuronal activation.

Ephys characterization of FeRIC channels

To characterize and validate TRPV4^{FeRIC} and TMEM16A^{FeRIC} as magnetic actuators in the FeRIC technique, we performed patch-clamp experiments using N2a cells. This strategy allowed us to overcome the inherent challenges associated with studying the biophysical properties of ion channels in neurons, i.e., the lack of space to clamp and poor voltage control in dendrites. First, we corroborated that RF does not affect the basal Ephys properties of mock-transfected N2a cells and N2a cells expressing TRPV4^{FeRIC}. Afterward, using the voltage-clamp configuration, we corroborated that RF decreases the Rm as a consequence of the activation of FeRIC channels. In N2a cells expressing TRPV4^{FeRIC}, RF stimulation for 5 min decreased the Rm to 61.5 ± 8.5% ($n = 13$ cells; $p < 0.05$) relative to the baseline (Fig. 9*B*). An off-target effect of RF was ruled out because, in mock-transfected N2a cells, RF did not change the Rm (95.5 ± 10.3%; $n = 6$ cells; $p = 0.71$; Fig. 9*A*). Additionally, we confirmed RF specifically acts on TRPV4^{FeRIC} because the RF-induced effect on the Rm was not observed in the presence of GSK219 (1 μM; 88.5 ± 8.1%; $n = 8$ cells; $p = 0.38$; Fig. 9*C*). Moreover, we corroborated that the RF-induced effects in the cells' bioelectrical properties were dependent on the ion flux through TRPV4^{FeRIC}. When the channel was mutated to be nonconductive (M680D/ΔK675), RF did not affect the Rm (111.5 ± 4.2%; $n = 8$ cells; $p = 0.68$; Fig. 9*D*). Finally, the RF effects on the membrane's electric properties were replicated with the TRPV4 agonist GSK1016790A (GSK101, 1 μM), which decreased the Rm to 60.7 ± 12.3% ($n = 6$; $p < 0.05$) relative to the baseline. This effect was inhibited with GSK219 (113.0 ± 11.6%; $n = 10$ cells; Fig. 9*E,F*). These results indicate that RF activates TRPV4^{FeRIC} channels, decreasing the Rm. Consistently, RF also decreased the Rm to 62.8 ± 10.4% ($n = 6$ cells; $p < 0.05$) in N2a cells expressing TMEM16A^{FeRIC}.

To further verify the activation of FeRIC channels with RF and gain insights into their biophysical properties, we assessed the effects of RF on membrane currents in N2a cells expressing TRPV4^{FeRIC}. Using the voltage-clamp configuration ($V_h = -60$ mV), we measured the mean amplitude in picoampere, the total time of the activated inward currents in seconds, and estimated the charges carried before (basal), during (RF), and after RF (post-RF) stimulation. In basal conditions, N2a cells expressing TRPV4^{FeRIC} showed infrequent inward currents with an amplitude of 3.6 ± 0.25 pA, a total time duration of 8.5 ± 2.3 s, and a total carried charge of 33.1 ± 9.1 pA•s ($n = 7$ cells; Fig. 9*G,I*). Compared with the baseline, RF (180 MHz and 1.6 μT for 5 min) increased the inward currents (3.7 ± 0.25 pA, 9.4 ± 2.1 s, 36.6 ± 8.3 pA•s; $n = 7$ cells) and reached a statistically significant difference in the post-RF period (post-RF: 4.1 ± 0.27 pA, 14.4 ± 3.4 s, 58.8 ± 12 pA•s; $p < 0.05$; $n = 7$; Fig. 9*G,I*). The RF effects on the membrane currents were blocked by GSK219 ($n = 7$; Fig. 9*H,J*). The RF-induced currents mediated by TRPV4^{FeRIC} were transient, with varying durations, and returned to the basal level ~5 min after RF stimulation was turned off. These observations suggest that RF does not activate all available TRPV4^{FeRIC} channels simultaneously and that the RF-produced stimuli are not cleared immediately after RF is removed. Remarkably, the inward currents mediated by TRPV4^{FeRIC} are similar to those observed when native TRPV4 is activated by endogenous lipids (Watanabe et al., 2003). To estimate the unitary conductance of TRPV4^{FeRIC}, we performed a nonstationary noise analysis (see Materials and Methods) of

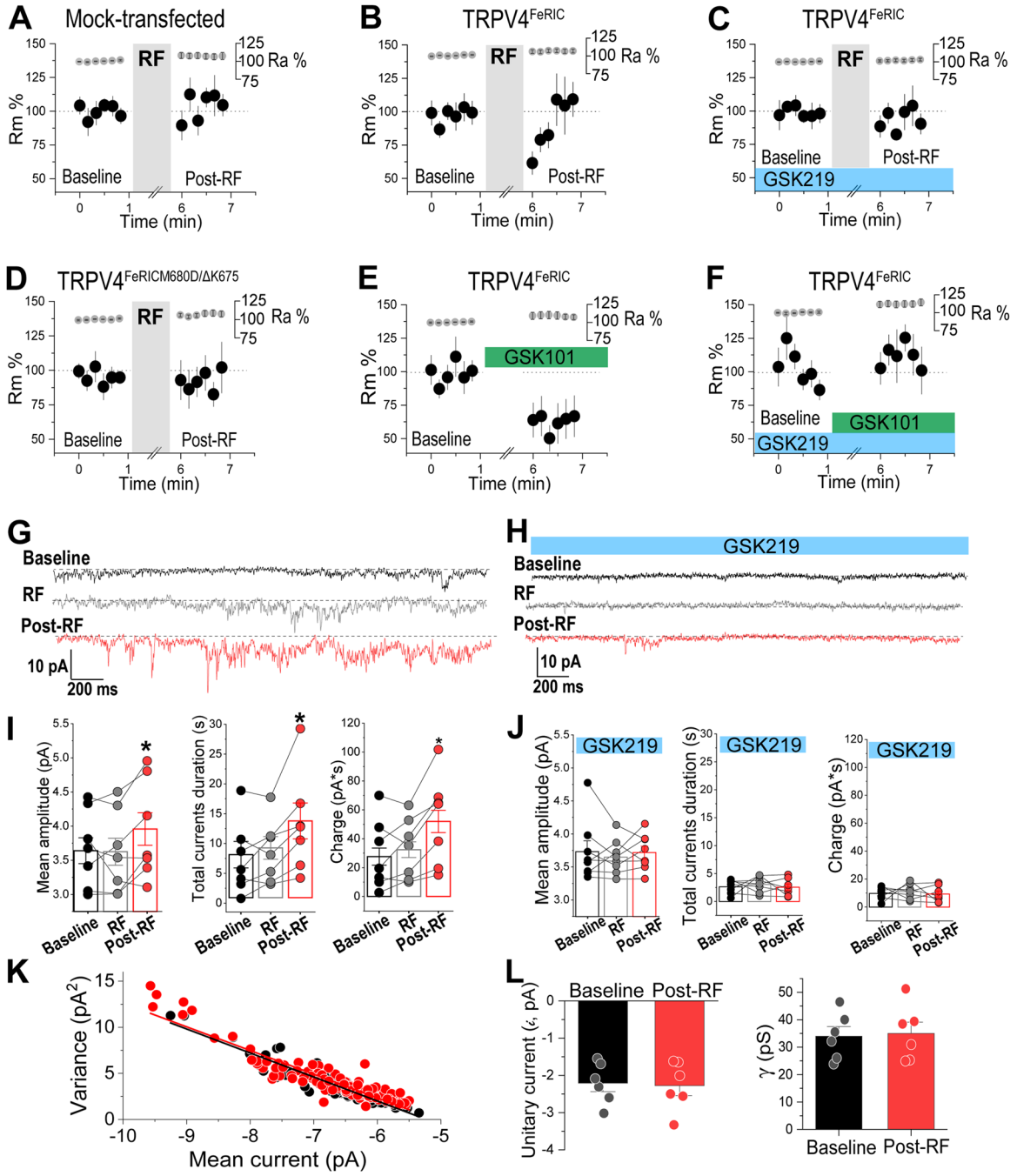

Figure 9. Ephys evidence of RF-induced activation of TRPV4 coupled with ferritin. ***A–F***, Time course of the average changes (±SEM) in the Rm and Ra from mock-transfected N2a cells ($n = 6$ cells) or N2a cells expressing TRPV4^{FeRIC} ($n = 13$ cells) or the nonconductive TRPV4^{FeRIC} (M680D/ΔK675, $n = 8$ cells) before and following RF or GSK101 (1 μM, $n = 6$ cells) stimulation. In separate series of experiments, cells were treated with the TRPV4 antagonist GSK219 (1 μM) before (***C***, $n = 8$ cells) RF or (***F***, $n = 10$ cells) GSK101 stimulation. ***G,H***, Representative whole-cell currents before RF (baseline, black), during RF (180 MHz and 1.6 μT, gray), and in the post-RF period (red) from N2a cells expressing TRPV4^{FeRIC} in the (***G***) absence or (***H***) the presence of GSK219. ***I,J***, Quantitative assessment of membrane current properties in N2a cells expressing TRPV4^{FeRIC} during baseline, RF, and post-RF periods in the absence (***I***, $n = 7$ cells) or presence (***J***, $n = 7$ cells) of GSK219. To analyze the currents, we used the automated event detection search algorithm in pClamp11 software, setting a threshold of 2.5 pA amplitude and a minimum of temporal length of 1 ms. The reported amplitude corresponds to the average event value, not the maximum (peak). ***K***, Current–variance relationships during baseline (black) and in the post-RF (red) period ($n = 7$ cells). Data were fit using the equation for the nonstationary noise analysis (see Materials and Methods). ***L***, Average unitary current (i) and unitary conductance (γ) in the baseline and in the post-RF period ($n = 7$ cells). Significance was determined using a two-tailed Student's t test and a two-way ANOVA followed by the Holm–Sidak multiple comparisons test. Where applicable, $^*p < 0.05$ was considered a statistically significant difference.

the whole-cell inward currents recorded in N2a cells expressing TRPV4^{FeRIC}. In this analysis, the relationship between the mean current amplitude (I) and the variance of the currents (σ^2) is used to estimate the ion channels' unitary current (i) and unitary conductance (γ; Fig. 9*K*; Sigworth, 1980; Traynelis and Jaramillo, 1998; Alvarez et al., 2002; Lingle, 2006; Hartveit and Veruki, 2007). In our experimental conditions, the estimated i for TRPV4^{FeRIC} was −2.2 ± 0.22 pA in the baseline and −2.3 ± 0.26 pA in the post-RF period. Using these values, the estimated γ of TRPV4^{FeRIC} was 34 ± 3.48 pS in the baseline and 35 ± 4.1 pS in the post-RF period (Fig. 9*L*). The estimated TRPV4^{FeRIC} conductance (γ) is similar to that reported for the WT TRPV4, which

range from 30 to 60 pS for inward currents (Voets et al., 2002; Plant and Strotmann, 2007). We did not observe differences when comparing the i or γ of TRPV4^{FeRIC} before or after RF stimulation ($p = 0.79$; $n = 7$ cells; Fig. 9*L*), suggesting that the RF-induced inward currents are due to an increase in the open channel probability of TRPV4^{FeRIC}. These findings provide further evidence supporting the validity of FeRIC as a tool for activating ferritin-coupled ion channels to manipulate the bioelectrical properties of diverse cell types, including neurons.

Discussion

Here, we obtained direct evidence for validating ferritin-based magnetogenetics, demonstrating the activation of ion channels coupled with ferritin under RF magnetic field stimulation. Specifically, we validated FeRIC as an approach that allows for the remote control of neurons' bioelectrical properties by activating the nonselective cation channel TRPV4 and the chloride-permeable channel TMEM16A. In neurons expressing TRPV4^{FeRIC}, RF depolarizes the membrane potential, decreases the Rm, and increases the spiking frequency. Conversely, in neurons expressing TMEM16A^{FeRIC}, RF hyperpolarizes the membrane potential and inhibits both the spontaneous and evoked spiking frequencies.

Several studies have reported the use of magnetic actuators, such as TRPV1 and TRPV4, coupled with ferritin to control cell activity using static and RF magnetic fields (Stanley et al., 2015, 2016; Wheeler et al., 2016; Hutson et al., 2017; Duret et al., 2019; Hernández-Morales et al., 2020, 2021). In this study, the objective was to validate FeRIC as a method for magnetically activating ferritin-coupled ion channels and modulating neurons' bioelectrical properties by integrating Ephys recordings with Ca^{2+} and voltage imaging. Previously, the confirmation of RF-induced activation of ferritin-coupled channels using Ephys was hindered by the lack of compatibility between the Ephys and RF systems. Here, we reduced the RF electromagnetic interference by focally delivering the RF stimulus and using ferrite beads designed to block frequencies near 180 MHz in the coaxial cables. Remarkably, the insights gained here provide opportunities for improving the Ephys and RF compatibility, such as utilizing mini coils to localize the RF stimulus to cells of interest with minimal RF electromagnetic interference.

Solving the compatibility between the Ephys setup and the RF system allowed us to conduct Ephys recordings to corroborate the RF-induced activation of FeRIC channels, their biophysical properties, and the RF effects on the cells' bioelectrical properties. The estimated unitary conductance for TRPV4^{FeRIC} was ~34 pS, which is in the range of the reported conductance values for WT TRPV4 channels (Voets et al., 2002; Plant and Strotmann, 2007). Moreover, our results suggest that RF increases the TRPV4^{FeRIC} open channel probability, generating inward currents that are similar to those reported for TRPV4 activated with endogenous ligands such as anandamide, AA, and epoxyeicosatrienoic acid (Watanabe et al., 2003; Hernández-Morales et al., 2020, 2021). We corroborated that in neurons, RF and ferritin interaction triggers an oxidative process that produces some of those endogenous actuators, which are responsible for the activation of ferritin-coupled ion channels (Hernández-Morales et al., 2020). Notably, the effect of RF on Rm in Neuro2a cells is transient, lasting a few seconds (Fig. 9*B*), while the effect of RF on neuronal membrane potential persists for minutes (Fig. 4*C*). The limited antioxidant capability of neurons (Baxter and Hardingham, 2016; Qiu et al., 2020) could have caused the RF-induced ROS to take longer to be neutralized, which may have led to the prolonged stimulation of FeRIC channels in neurons, and not in Neuro2a cells. Another potential consequence of the limited ability of neurons to handle ROS, combined with their complex morphology comprising fine dendritic and axonal processes, is that RF-induced ROS could reach and affect the recombinant WT TRPV4 channels. Although our experiments did not reveal any effect, additional examination is needed to confirm or dismiss any RF effect on WT channels.

It is important to note that the FeRIC technique is not suitable for instantaneously controlling neurons on the order of milliseconds. RF gradually changes the neuronal membrane potential and modifies the spiking frequency of neurons expressing FeRIC channels on the minute scale. Our results contrast with previous studies that report immediate triggering of APs in neurons expressing TRPV1 tagged with ferritin (Stanley et al., 2016) or TRPV4 fused with ferritin (Wheeler et al., 2016) upon stimulation with static magnetic fields. However, these reports did not provide further characterization of the magnetic activation of the ferritin-coupled TRPV channels with RF. As of now, there is no evidence supporting that native TRPV4 channels directly initiate APs. In hippocampal neurons, these channels play a role in regulating the resting membrane potential and neuronal excitability (Shibasaki et al., 2007, 2015). Under physiological conditions, TRPV4 exhibits constitutive activation at the body temperature of 37°C, resulting in a depolarized membrane potential. This condition enhances the neurons' readiness to reach the AP threshold in response to other electrical or synaptic inputs (Shibasaki et al., 2007). Likely, a similar effect is produced by RF-induced activation of TRPV4^{FeRIC} in hippocampal neurons.

A limitation of FeRIC is that controlling neuronal excitability is slow when compared with the millisecond-scale control offered by optogenetics. These slower dynamics can be attributed to the intrinsic activation kinetics when TRPV4 is activated with lipids, which attests to the complex biochemical mechanism that underlies ferritin-based magnetogenetics. FeRIC is therefore suited for addressing problems that do not require manipulation of cells at a millisecond-order timescale, e.g., studying the effects of tonic transmission or plasticity in the functioning of the neuronal circuitry.

The main advantages of FeRIC are the use of magnetic fields and endogenous ferritin as an RF transducer. Magnetic fields penetrate effectively through the entire nervous system, allowing for the development of noninvasive tools (Young et al., 1980). In comparison, optogenetic approaches require invasive procedures for light delivery and are limited by light scattering and poor penetration into tissues (Packer et al., 2013). Furthermore, magnetic fields interact weakly with biological tissues and thus avoid off-target effects, while optogenetics suffers from undesired increases in neuronal spiking frequency (Stujenske et al., 2015) that are caused by high-power light raising the temperature in surrounding tissues (Picot et al., 2018). Using endogenous ferritin as the RF transducer prevents the cytotoxic effects and disturbance of cellular iron homeostasis observed with recombinant ferritin overexpression (Nie et al., 2005).

In conclusion, we show that the FeRIC technique allows the control of neuronal bioelectrical properties. The FeRIC technique opens opportunities to interrogate the relationship between neuronal excitability and diverse brain functions in freely moving experimental models.

Data Availability Statement

All data are available in the main text. The codes generated during this study are available at GitHub: https://github.com/LiuCLab/FeRIC. The cDNA sequence of TRPV4^{FeRIC} is available at GenBank with the identifier TRPV4^{FeRIC}: MT025942 (https://

www.ncbi.nlm.nih.gov/nuccore/). The statistical analysis as well as the Ephys and Ca^{2+} imaging analysis files is available at Mendeley Data (https://doi.org/10.17632/y3gbz9s9rp.1).

References

Analog Devices Inc. (1993) *System applications guide.* Norwood, Massachusetts: Analog Devices, Inc.

Alvarez O, Gonzalez C, Latorre R (2002) Counting channels: a tutorial guide on ion channel fluctuation analysis. Adv Physiol Educ 26:327–341.

Baxter PS, Hardingham GE (2016) Adaptive regulation of the brain's antioxidant defences by neurons and astrocytes. Free Radic Biol Med 100:147–152.

Benítez-Angeles M, Morales-Lázaro SL, Juárez-González E, Rosenbaum T (2020) TRPV1: structure, endogenous agonists, and mechanisms. Iran J Med Sci 21:3421.

Brier MI, Mundell JW, Yu X, Su L, Holmann A, Squeri J, Zhang B, Stanley SA, Friedman JM, Dordick JS (2020) Uncovering a possible role of reactive oxygen species in magnetogenetics. Sci Rep 10:13096.

Caterina MJ, Rosen TA, Tominaga M, Brake AJ, Julius D (1999) A capsaicin-receptor homologue with a high threshold for noxious heat. Nature 398: 436–441.

Darby WG, Grace MS, Baratchi S, McIntyre P (2016) Modulation of TRPV4 by diverse mechanisms. Int J Biochem Cell Biol 78:217–228.

Davis HC, Kang S, Lee J-H, Shin T-H, Putterman H, Cheon J, Shapiro MG (2020) Nanoscale heat transfer from magnetic nanoparticles and ferritin in an alternating magnetic field. Biophys J 118:1502–1510.

Dulin NO (2020) Calcium-activated chloride channel ANO1/TMEM16A: regulation of expression and signaling. Front Physiol 11:590262.

Duret G, Polali S, Anderson ED, Bell AM, Tzouanas CN, Avants BW, Robinson JT (2019). Magnetic entropy as a proposed gating mechanism for magnetogenetic ion channels. Biophys J 116, 454–468.

Eisenman LN, Emnett CM, Mohan J, Zorumski CF, Mennerick S (2015) Quantification of bursting and synchrony in cultured hippocampal neurons. J Neurophysiol 114:1059–1071.

Friedrich J, Zhou P, Paninski L (2017) Fast online deconvolution of calcium imaging data. PLoS Comput Biol 13:e1005423.

Giovannucci A, et al. (2019) CaImAn an open source tool for scalable calcium imaging data analysis. Elife 8:e38173.

Grant MC, Boyd SP (2008) Graph implementations for nonsmooth convex programs. In: *Recent advances in learning and control* (Blondel VD, Boyd SP, Kimura H eds). pp 95–110. London: Springer.

Hartveit E, Veruki ML (2007) Studying properties of neurotransmitter receptors by non-stationary noise analysis of spontaneous postsynaptic currents and agonist-evoked responses in outside-out patches. Nat Protoc 2:434–448.

Hernández-Morales M, Han V, Kramer RH, Liu C (2021) Evaluating methods and protocols of ferritin-based magnetogenetics. iScience 24:103094.

Hernández-Morales M, Shang T, Chen J, Han V, Liu C (2020) Lipid oxidation induced by RF waves and mediated by ferritin iron causes activation of ferritin-tagged ion channels. Cell Rep 30:3250–3260.e7.

Huang Y-L, Walker AS, Miller EW (2015) A photostable silicon rhodamine platform for optical voltage sensing. J Am Chem Soc 137:10767–10776.

Hutson MR, et al. (2017) Temperature-activated ion channels in neural crest cells confer maternal fever-associated birth defects. Sci Signal 10: eaal4055.

Kole K, Zhang Y, Jansen EJR, Brouns T, Bijlsma A, Calcini N, Yan, Lantyer, Celikel (2019) Assessing the utility of Magneto to control neuronal excitability in the somatosensory cortex. Nat Neurosci 23:1044–1046.

Lingle CJ (2006) Empirical considerations regarding the use of ensemble-variance analysis of macroscopic currents. J Neurosci Methods 158: 121–132.

Meister M (2016) Physical limits to MAGNETOgenetics. Elife 5:e17210.

Meyer F (1994) Topographic distance and watershed lines. Signal Process 38: 113–125.

Mundell JW, Brier MI, Orloff E, Stanley SA, Dordick JS (2024) Alternating magnetic fields drive stimulation of gene expression via generation of reactive oxygen species. iScience 27:109186.

Nie G, Sheftel AD, Kim SF, Ponka P (2005) Overexpression of mitochondrial ferritin causes cytosolic iron depletion and changes cellular iron homeostasis. Blood 105:2161–2167.

Packer AM, Roska B, Häusser M (2013) Targeting neurons and photons for optogenetics. Nat Neurosci 16:805–815.

Picot A, et al. (2018) Temperature rise under two-photon optogenetic brain stimulation. Cell Rep 24:1243–1253.e5.

Plant TD, Strotmann R (2007) TRPV4: a multifunctional nonselective cation channel with complex regulation. In: *TRP ion channel function in sensory transduction and cellular signaling cascades* (Liedtke WB, Heller S, eds), Boca Raton, FL: CRC Press/Taylor and Francis.

Pnevmatikakis EA, et al. (2016) Simultaneous denoising, deconvolution, and demixing of calcium imaging data. Neuron 89:285–299.

Qiu J, Dando O, Febery JA, Fowler JH, Chandran S, Hardingham GE (2020) Neuronal activity and its role in controlling antioxidant genes. Int J Mol Sci 21:1933.

Schenck JF (2000) Safety of strong, static magnetic fields. J Magn Reson Imaging 12:2–19.

Schreiber R, Buchholz B, Kraus A, Schley G, Scholz J, Ousingsawat J, Kunzelmann K (2019) Lipid peroxidation drives renal cyst growth in vitro through activation of TMEM16A. J Am Soc Nephrol 30:228–242.

Schreiber R, Ousingsawat J, Wanitchakool P, Sirianant L, Benedetto R, Reiss K, Ishizaki Y (2018) Regulation of TMEM16A/ANO1 and TMEM16F/ANO6 ion currents and phospholipid scrambling by Ca^{2+} and plasma membrane lipid: regulation of TMEM16A and TMEM16F by Ca^{2+} and lipid. J Physiol 596:217–229.

Shibasaki K, Sugio S, Takao K, Yamanaka A, Miyakawa T, Tominaga M, Ishizaki Y (2015) TRPV4 activation at the physiological temperature is a critical determinant of neuronal excitability and behavior. Pflugers Arch 467:2495–2507.

Shibasaki K, Suzuki M, Mizuno A, Tominaga M (2007) Effects of body temperature on neural activity in the hippocampus: regulation of resting membrane potentials by transient receptor potential vanilloid 4. J Neurosci 27:1566–1575.

Sigworth FJ (1980) The variance of sodium current fluctuations at the node of Ranvier. J Physiol 307:97–129.

Stanley SA, Kelly L, Latcha KN, Schmidt SF, Yu X, Nectow AR, Sauer J, Dyke JP, Dordick JD, Friedman JM (2016) Bidirectional electromagnetic control of the hypothalamus regulates feeding and metabolism. Nature 531: 647–650.

Stanley SA, Sauer J, Kane RS, Dordick JS, Friedman JM (2015) Remote regulation of glucose homeostasis in mice using genetically encoded nanoparticles. Nat Med 21:92–98.

Stujenske JM, Spellman T, Gordon JA (2015) Modeling the spatiotemporal dynamics of light and heat propagation for in vivo optogenetics. Cell Rep 12:525–534.

Sun Z, Williams DJ, Xu B, Gogos JA (2018) Altered function and maturation of primary cortical neurons from a 22q11.2 deletion mouse model of schizophrenia. Transl Psychiatry 8:85.

Traynelis SF, Jaramillo F (1998) Getting the most out of noise in the central nervous system. Trends Neurosci 21:137–145.

Voets T, Prenen J, Vriens J, Watanabe H, Janssens A, Wissenbach U, Bödding M, Droogmans G, Nilius B (2002) Molecular determinants of permeation through the cation channel TRPV4. J Biol Chem 277:33704–33710.

Vogelstein JT, Packer AM, Machado TA, Sippy T, Babadi B, Yuste R, Paninski L (2010) Fast nonnegative deconvolution for spike train inference from population calcium imaging. J Neurophysiol 104:3691–3704.

Walker AS, Raliski BK, Karbasi K, Zhang P, Sanders K, Miller EW (2021) Optical spike detection and connectivity analysis with a far-red voltage-sensitive fluorophore reveals changes to network connectivity in development and disease. Front Neurosci 15:643859.

Wang G, Zhang P, Mendu SK, Wang Y, Zhang Y, Kang X, Desai BN, Zhu JJ (2019) Revaluation of magnetic properties of Magneto. Nat Neurosci 23: 1047–1050.

Watanabe H, Vriens J, Prenen J, Droogmans G, Voets T, Nilius B (2003) Anandamide and arachidonic acid use epoxyeicosatrienoic acids to activate TRPV4 channels. Nature 424:434–438.

Wheeler, MA, et al. (2016) Genetically targeted magnetic control of the nervous system. Nat Neurosci 19, 756–761.

Xu F-X, Zhou L, Wang X-T, Jia F, Ma K-Y, Wang N, Lin L, Xu FQ, Shen Y (2019) Magneto is ineffective in controlling electrical properties of cerebellar Purkinje cells. Nat Neurosci 23:1041–1043.

Young JH, Wang M-T, Brezovich IA (1980) Frequency/depth-penetration considerations in hyperthermia by magnetically induced currents. Electron Lett 16:358.